Inorganic Chemistry

Article

pubs.acs.org/IC

Aerobic and Hydrolytic Decomposition of Pseudotetrahedral Nickel Phenolate Complexes

Tapash Deb,[†] Gregory T. Rohde,[‡] Victor G. Young, Jr.,[‡] and Michael P. Jensen*,[†]

[†]Department of Chemistry and Biochemistry, Ohio University, Athens, Ohio 45701, United States

[‡]X-ray Crystallographic Facility, Department of Chemistry, University of Minnesota, Minneapolis, Minnesota 55455, United States

Supporting Information

ABSTRACT: Pseudotetrahedral nickel(II) phenolate complexes $Tp^{R,Me}$Ni-OAr ($Tp^{R,Me}$ = hydrotris(3-R-5-methylpyrazol-1-yl)borate; R = Ph {**1a**}, Me {**1b**}; OAr = O-2,6-$^{i}Pr_2C_6H_3$) were synthesized as models for nickel-substituted copper amine oxidase apoenzyme, which utilizes an N_3O (i.e., His_3Tyr) donor set to activate O_2 within its active site for oxidative modification of the tyrosine residue. The bioinspired synthetic complexes **1a**,**b** are stable in dilute CH_2Cl_2 solutions under dry anaerobic conditions, but they decompose readily upon exposure to O_2 and H_2O. Aerobic decomposition of **1a** yields a range of organic products consistent with formation of phenoxyl radical, including 2,6-diisopropyl-1,4-benzoquinone, 3,5,3′,5′-tetraisopropyl-4,4′-diphenodihydroquinone, and 3,5,3′,5′-tetraisopropyl-4,4′-diphenoquinone, which requires concurrent O_2 reduction. The dimeric product complex di[hydro{bis(3-phenyl-5-methylpyrazol-1-yl)(3-*ortho*-phenolato-5-methylpyrazol-1-yl)borato}nickel(II)] (**2**) was obtained by *ortho* C−H bond hydroxylation of a 3-phenyl ligand substituent on **1a**. In contrast, aerobic decomposition of **1b** yields a dimeric complex $[Tp^{Me,Me}Ni]_2(\mu\text{-}CO_3)$ (**3**) with unmodified ligands. However, a unique organic product was recovered, assigned as 3,4-dihydro-3,4-dihydroxy-2,6-diisopropylcyclohex-5-enone on the basis of ^{1}H NMR spectroscopy, which is consistent with dihydroxylation (i.e., addition of H_2O_2) across the *meta* and *para* positions of the phenol ring. Initial hydrolysis of **1b** yields free phenol and the known complex $[Tp^{Me,Me}Ni(\mu\text{-}OH)]_2$, while hydrolysis of **1a** yields an uncharacterized intermediate, which subsequently rearranges to the new sandwich complex $[(Tp^{Ph,Me})_2Ni]$ (**4**). Autoxidation of the released phenol under O_2 was observed, but the reaction was slow and incomplete. However, both **4** and the *in situ* hydrolysis intermediate derived from **1a** react with added H_2O_2 to form **2**. A mechanistic scheme is proposed to account for the observed product formation by convergent oxygenation and hydrolytic autoxidation pathways, and hypothetical complex intermediates along the former were modeled by DFT calculations. All new complexes (i.e., **1a**,**b** and **2**−**4**) were fully characterized by FTIR, ^{1}H NMR, and UV−vis−NIR spectroscopy and by X-ray crystallography.

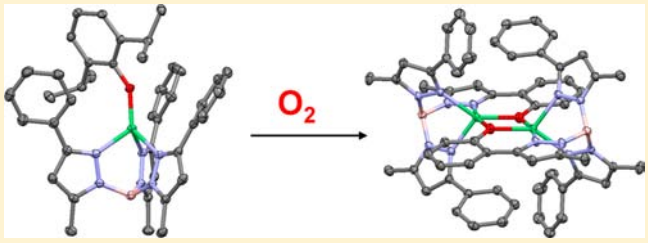

1.0. INTRODUCTION

Dioxygen activation is fundamentally important in catalysis and bioinorganic chemistry. Significant work has been directed at enzymatic and biomimetic iron and copper centers that react with O_2,[1−10] yet nickel/O_2 chemistry and biochemistry are relatively limited in scope. Only one nickel-dependent oxidase enzyme has been characterized so far, namely acireductone dioxygenase (Ni-ARD),[11] for which functional turnover modeling has been elicited from synthetic Ni(II) complexes of aryl-appended tris(pyridylmethyl)amine (TPA) ligands.[12] Synthetic Ni(II) complexes of electron-rich tris(oximato)amine and diamido macrocyclic ligands catalyze aerobic substrate oxidations,[13,14] and macrocyclic complexes of Ni(II) catalyze oxygen atom transfer from suitable precursors to organic substrates.[15−17] Stoichiometric oxygenation reactions of Ni(II)−thiolato complexes are also known.[18] Superoxo,[19−26] peroxo,[25−31] and oxo[31−42] complexes supported by diketimine (nacnac),[21,22,43] TPA,[24,25,27,35,36,40−42] hydrotris(pyrazolyl)borate (Tp),[30−34] tetraazamacrocycles (e.g., tetramethylcyclam, tmc),[20,26,28,29] and related polydentate ligands[19,23,37−39,44] have been prepared, either by stoichiometric O_2 addition to Ni(I),[19−23,28,29,37−39,43−45] or H_2O_2 addition to Ni(II) precursors.[20,24−27,32−36,40−42] No biological role for nickel has been established in humans, but nickel toxicology is of interest.[46−48] Elevated intracellular levels are associated with mutagenesis, and one proposed mechanism involves catalytic depletion of cellular antioxidants, which implies formation of reduced oxygen species.[48]

Copper amine oxidases (CAOs) activate O_2 to effect post-translational oxidation of an active-site tyrosine residue in the expressed apoenzyme to a catalytically essential 2,4,5-trihydroxyphenylalanine quinone (i.e., TPQ) cofactor in the active holoenzyme (Scheme 1).[49−52] Our present work was inspired by reports that TPQ biogenesis is also observed in apoenzymes reconstituted with nickel, comprising a second example of biological dioxygenase activity for this metal.[53,54] X-ray crystallography revealed a pseudotetrahedral N_3O donor set

Received: March 14, 2012
Published: June 15, 2012

Scheme 1

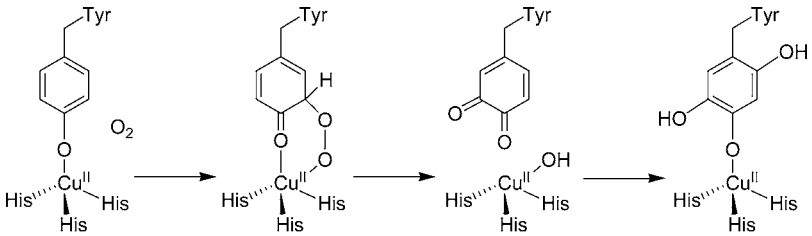

in the apoenzyme active site, derived from three histidine imidazoles and one tyrosine side chain, which is the TPQ precursor.[49] Following active-site binding of copper and O_2, a Cu(II)−phenolate LMCT species intermediate absorbing at 350 nm was observed, which exhibited isosbestic decay to a 480 nm chromophore characteristic of TPQ in the mature holoenzyme.[50] Other consensus intermediates include an unobserved Cu(II)−peroxyquinone complex,[49−52] which undergoes heterolysis to a structurally characterized dopaquinone intermediate,[49] but the mechanistic details of the O_2 activation step(s) remain to be elucidated.

TpCu(II)−OAr complexes with pseudotetrahedral N_3O ligand fields have been reported as CAO models,[52,55] wherein the Tp ligand models the facial array of imidazole donors and the phenolate coligand completes an N_3O ligand field akin to the CAO active site. However, the complexes $Tp^{tBu,R}Cu-O-C_6H_4$-4-F (R = ^{i}Pr, ^{t}Bu) were unreactive with O_2,[52] while analogues with *ortho*-disubstituted phenolates decomposed even under inert atmosphere.[55] Similar behavior was also reported for (nacnac)Cu−OAr complexes.[56] Compared to the TpCu−OAr complexes, nickel analogues might be expected to exhibit higher stability, owing to relatively cathodic Ni(I/II) redox couples, but such complexes have not been reported.

Building on previous work with O_2-sensitive Ni(II)−arylthiolate complexes $Tp^{R,Me}Ni-SAr$,[57−61] we report herein the bioinspired complexes $Tp^{R,Me}Ni-OAr$ ($Tp^{R,Me}$ = hydrotris{3-R-5-Me-pyrazol-1-yl}borate;[62,63] R = Ph (**1a**), Me (**1b**); Ar = 2,6-^{i}Pr$_2$C$_6$H$_3$). These are thermally stable in anaerobic solutions but decompose under O_2. Observed organic products were consistent with formation of phenoxyl radical and concurrent reduction of O_2, and subsequent aromatic oxidation chemistry was observed, at either a 3-Ph pyrazole substituent of **1a** or the phenolato ring of **1b**. Taken together, these reactions are analogous to oxidase and monooxygenase activities leading to TPQ biogenesis in nickel-substituted apo-CAO, although the reaction mechanism remains uncertain. Pro-oxidant chemistry through formation of reduced oxygen species catalyzed by interaction of nickel with biological phenols and thiols would also be of interest with respect to the toxicology of the metal.[48] Recently, a biomimetic Cu(II) complex was reported to react with O_2 and transform a phenol ligand substituent into a TPQ analogue.[64] Attention is called to analogous intramolecular hydroxylations of ligand substituents upon addition of H_2O_2 to Ni(II) complexes[40−42] and oxidative transformations of substituted phenols by a discrete (nacnac)NiO_2 complex.[22]

2.0. EXPERIMENTAL SECTION

All materials were obtained from commercial vendors and used as received, except for drying of solvents by routine techniques. Syntheses were carried out under prepurified argon, either in a glovebox (MBraun Unilab) or using Schlenk techniques. $Tp^{R,Me}NiCl$ complexes (R = Me, Ph) were prepared from anhydrous $NiCl_2$ and $TlTp^{R,Me}$ in MeOH/CH_2Cl_2 as previously described (***Caution***: *Thallium salts are extremely toxic and must be properly handled and disposed of!*).[58,59,65,66] 2,6-Diisopropylphenol (Alfa Aesar) was reacted with NaH in toluene to afford the sodium salt of the conjugate base. ^{1}H NMR data were recorded on Bruker 300 Ultrashield and Varian Unity 500 spectrometers and processed using the MestReNova software suite (Mestrelab Research, Santiago de Compostela, Spain); spectra were referenced internally to residual $CHCl_3$, $CHDCl_2$, and $C_6D_5CHD_2$ solvents (7.24, 5.32, and 2.08 ppm, respectively). Solution magnetic moments were determined by the Evans NMR method.[67] FT-IR spectra were recorded from KBr pellets on a Thermo-Electron Nicolet 380 spectrophotometer. UV−vis−NIR spectra were recorded on an Agilent HP-8453 diode-array spectrophotometer. Elemental analyses were performed by Atlantic Microlabs (Norcross, GA). Spectroscopic data for complexes **1a,b** are shown in Figures S1−S8 of the Supporting Information and summarized below.

2.1. Synthesis of $Tp^{Ph,Me}Ni-O-2,6-^iPr_2C_6H_3$ (1a). A sample of $Tp^{Ph,Me}NiCl$ (150 mg, 0.26 mmol) dissolved in dichloromethane (10 mL) was added to a slurry of NaO-2,6-^{i}Pr$_2$C$_6$H$_3$ (57 mg, 0.29 mmol) in CH_2Cl_2 (10 mL). The color changed from pale pink to dark green when the solutions were combined. After stirring for 2.0 h, the solution was filtered and evaporated to dryness. The filtrate was redissolved in a minimal amount of CH_2Cl_2, and green crystals were obtained by slow diffusion of *n*-hexane at −30 °C. Yield: 171 mg (0.24 mmol, 92%). Anal. Calcd (found) for $C_{42}H_{45}BN_6NiO$, **1a**: C, 70.13 (70.27); H, 6.31 (5.88); N, 11.68 (11.69). ^{1}H NMR (CD_2Cl_2, 293 K; δ, ppm): 74.1 (3H, 4-pz); 42 (2H, br, −C*H*Me$_2$); 39.3 (2H, *meta*); 14.4 (6H, br, 3-*ortho*); 8.9 (3H, 3-*para*); 7.1 (6H, 3-*meta*); 2.7 (12H, br, −CH*Me*$_2$); −2.2 (9H, 5-Me); −19.9 (1H, B-*H*); −43.4 (1H, *para*). μ_{eff} = 2.72 μ_B ($CDCl_3$, 293 K). UV−vis−NIR (CH_2Cl_2; λ_{max}, nm; ε, M^{-1} cm^{-1}): 476 (1900); 612 (800); 995 (200). IR (KBr, cm^{-1}): 2543, ν(B−H).

2.2. Synthesis of $Tp^{Me,Me}Ni-O-2,6-^iPr_2C_6H_3$ (1b). A sample of $Tp^{Me,Me}NiCl$ (150 mg, 0.38 mmol) dissolved in dichloromethane (10 mL) was added to a slurry of NaO-2,6-^{i}Pr$_2$C$_6$H$_3$ (75 mg, 0.38 mmol) in CH_2Cl_2 (10 mL). The color changed from pale pink to dark orange immediately after the solutions were combined. After stirring for 2.0 h, the solution was filtered and evaporated to dryness. The filtrate was redissolved in a minimal amount of CH_2Cl_2, and orange crystals were obtained by slow diffusion of *n*-hexane at −30 °C. Yield: 186 mg (0.35 mmol, 91%). Anal. Calcd (found) for $C_{27}H_{39}BN_6NiO$, **1b**: C, 60.83 (60.79); H, 7.37 (7.36); N, 15.76 (15.50). ^{1}H NMR (CD_2Cl_2, 293 K; δ, ppm): 76.9 (3H, 4-pz); 30.3 (2H, *meta*); 26.5 (2H, br, −C*H*Me$_2$); 3.9 (12H, br, −CH*Me*$_2$); −0.8 (9H, 3-M*e*); −6.6 (9H, 5-Me); −19.0 (1H, B-*H*); −28.0 (1H, *para*). ^{1}H NMR ($C_6D_5CD_3$, 293 K; δ, ppm): 75.5 (3H, 4-pz); 31.5 (2H, *meta*); 28.0 (2H, br, −C*H*Me$_2$); 4.0 (12H, br, −CH*Me*$_2$); −1.3 (9H, 3-M*e*); −6.5 (9H, 5-Me); −19.2 (1H, B-*H*); −29.5 (1H, *para*). μ_{eff} = 3.09 μ_B ($CDCl_3$, 293 K). UV−vis−NIR (CH_2Cl_2; λ_{max}, nm; ε, M^{-1} cm^{-1}): 326 (sh, 700); 421 (sh, 770); 449 (1000); 514 (330); 810 (80); 940 (120). IR (KBr, cm^{-1}): 2523, ν(B−H).

2.3. Synthesis of Organic Standards. 3,5,3′,5′-Tetraisopropyl-4,4′-diphenoquinone and 2,6-diisopropyl-1,4-benzoquinone were prepared by oxidation of 2,6-diisopropylphenol according to literature procedures;[68] reduced dihydroquinones were then obtained by sequential addition of dilute hydrochloric acid and zinc dust to solutions of quinone in aqueous methanol, followed by filtration and removal of solvent under vacuum. Spectroscopic data are summarized below and shown in Figures S9−S22 of the Supporting Information;

Table 1. Summary of X-ray Crystallography

compound	$Tp^{Ph,Me}Ni-O-2,6-^{i}Pr_2C_6H_3$ (**1a**)	$Tp^{Me,Me}Ni-O-2,6-^{i}Pr_2C_6H_3$ (**1b**)	$[(Tp^{Ph,Me*})Ni]_2$ (**2**)	$[Tp^{Me,Me}]Ni_2(\mu\text{-}CO_3)$ (**3**)	$[(Tp^{Ph,Me})_2Ni]$ (**4**)
empirical formula	$C_{42}H_{45}BN_6NiO$	$C_{27}H_{39}BN_6NiO$	$C_{60}H_{54}B_2N_{12}Ni_2O_2$	$C_{31}H_{44}B_2N_{12}Ni_2O_3$	$C_{60}H_{56}B_2N_{12}Ni$
formula weight	719.36	533.16	1114.19	771.82	1025.50
temp (K)	123(2)	123(2)	173(2)	173(2)	173(2)
crystal system	triclinic	monoclinic	tetragonal	monoclinic	monoclinic
space group	$P\bar{1}$	$P2_1/n$	$P4_2/n$	$P2_1$	$C2/c$
a (Å)	10.7698(9)	8.803(1)	19.682(2)	8.053(5)	18.0500(9)
b (Å)	11.111(1)	29.373(3)	19.682(2)	30.94(2)	13.7439(7)
c (Å)	12.251(2)	10.630(1)	13.541(1)	8.073(5)	21.985(2)
α (deg)	84.405(1)	90	90	90	90
β (deg)	78.857(1)	91.832(1)	90	113.820(6)	111.505(1)
γ (deg)	65.717(1)	90	90	90	90
V (Å^3)	1845.8(3)	2747.2(5)	5245.5(8)	1840(2)	5074.3
Z	2	4	4	2	4
density (calc, g/cm^3)	1.294	1.289	1.411	1.393	1.342
absorption coefficient (mm^{-1})	0.568	0.737	0.776	1.073	0.437
crystal color, morphology	green, block	orange, irregular	green, needle	green, block	green, block
crystal size (mm)	0.22 × 0.12 × 0.10	0.25 × 0.12 × 0.05	0.45 × 0.12 × 0.10	0.45 × 0.12 × 0.10	1.13 × 1.07 × 0.44
reflections collected	22004	30891	60638	14999	28593
independent reflections (R_{int})	8349 (0.0310)	6280 (0.0751)	5365 (0.0500)	6484 (0.0528)	5818 (0.0221)
observed reflections	6959	4388	4145	5206	5209
data/restraints/parameters	8349/0/467	6280/0/339	5365/0/355	6484/1/464	5818/0/346
GoF	1.047	1.037	1.020	1.061	1.032
$R1$, $wR2$ [$I > 2\sigma(I)$]	0.0364, 0.0806	0.0476, 0.1056	0.0389/0.0983	0.0525, 0.1114	0.0308, 0.0776
$R1$, $wR2$ (all data)	0.0471, 0.0859	0.0803, 0.1190	0.0559/0.1088	0.0718, 0.1194	0.0356, 0.0805
difference peak, hole (e/Å^3)	0.596, −0.353	0.661, −0.503	0.436, −0.260	0.579, −0.627	0.268, −0.325

plots use a labeling scheme A−F, including a naphthalene standard (A) and others as indicated.

2.3.1. 2,6-Diisopropylphenol (B). ^{1}H NMR (300 MHz, $CDCl_3$, 293 K; δ, ppm): 7.05 (d, 7.6 Hz, 2H); 6.90 (t, 7.6 Hz, 1H); 4.76 (s, 1H); 3.15 (septet, 6.8 Hz, 2H); 1.27 (d, 6.8 Hz, 12H). UV−vis−NIR (CH_2Cl_2; λ_{max}, nm; ε, M^{-1} cm^{-1}): 273 (1600).

2.3.2. 2,6-Diisopropyl-1,4-benzoquinone (C). ^{1}H NMR (300 MHz, $CDCl_3$, 293 K; δ, ppm): 6.45 (s, 2H); 3.05 (septet, 6.9 Hz, 2H); 1.11 (d, 6.9 Hz, 12H). UV−vis−NIR (CH_2Cl_2; λ_{max}, nm; ε, M^{-1} cm^{-1}): 325 (320); 414 (40).

2.3.3. 2,6-Diisopropyl-1,4-benzodihydroquinone (D). ^{1}H NMR (300 MHz, $CDCl_3$, 293 K; δ, ppm): 6.52 (s, 2H), 4.60 (s, 1H); 4.43 (s, 1H); 3.11 (septet, 6.8 Hz, 2H); 1.22 (d, 6.8 Hz, 12H). UV−vis−NIR (CH_2Cl_2; λ_{max}, nm; ε, M^{-1} cm^{-1}): 289 (8400).

2.3.4. 3,5,3′,5′-Tetraisopropyl-4,4′-diphenoquinone (E). ^{1}H NMR (300 MHz, $CDCl_3$, 293 K; δ, ppm): 7.64 (s, 4H); 3.22 (septet, 6.9 Hz, 4H); 1.20 (d, 6.9 Hz, 24H). UV−vis−NIR (CH_2Cl_2; λ_{max}, nm; ε, M^{-1} cm^{-1}): 426 (71000).

2.3.5. 3,5,3′,5′-Tetraisopropyl-4,4′-diphenodihydroquinone (F). ^{1}H NMR (300 MHz, $CDCl_3$, 293 K; δ, ppm): 7.17 (s, 4H); 4.74 (s, 2H); 3.19 (septet, 6.9 Hz, 4H); 1.31 (d, 6.9 Hz, 24H). UV−vis−NIR (CH_2Cl_2; λ_{max}, nm; ε, M^{-1} cm^{-1}): 265 (17000).

2.4. Aerobic Decomposition of $Tp^{Ph,Me}Ni-O-2,6-^{i}Pr_2C_6H_3$ (1a): Isolation of $[(Tp^{Ph,Me*})Ni]_2$ (2). A sample of **1a** (96 mg, 0.13 mmol) was dissolved in CH_2Cl_2 (18 mL) and sealed in a vial with a rubber septum under argon. The solution was purged for approximately 5 s with a stream of O_2 gas flowing from a needle after passage through a column of CaH_2, anhydrous $CaSO_4$, and $MgSO_4$ to ensure removal of trace H_2O. The punctured septum was then covered with silicone grease to exclude atmospheric moisture. The green color of the solution slowly deepened on standing overnight. After 24 h, *n*-hexane was introduced by vapor diffusion. Green crystals of product complex **2**, identified as di[hydro{bis(3-phenyl-5-methylpyrazol-1-yl)(3-*ortho*-phenolato-5-methylpyrazol-1-yl) borato}nickel(II)], formed after standing for 3 days, and these were recovered by filtration (yield: 40 mg, 0.04 mmol, 53%); the organic coproducts remaining in the reddish-brown mother liquor were identified and quantified by independent synthesis and GC-MS (*vide infra*). The spectra of **2** are shown in Figures S30−S34 of the Supporting Information. Anal. Calcd (found) for $C_{60}H_{58}B_2N_{12}Ni_2O_4$, **2**·$2H_2O$: C, 62.65 (63.05); H, 5.08 (4.91); N, 14.61 (14.62). ^{1}H NMR ($CDCl_3$, 293 K; δ, ppm): 76.0 (1H); 64.6 (2H); 46.4 (1H); 30.2 (1H); −3.6 (6H); −10.2 (1H); −25.5 (1H); −30.4 (1H); plus unassigned peaks. μ_{eff} = 2.42 μ_B ($CDCl_3$, 293 K). UV−vis−NIR (CH_2Cl_2; λ_{max}, nm; ε, M^{-1} cm^{-1}): 268 (23000); 306 (sh, 8700); 317 (9000); 420 (3100); 598 (60); 755 (30); 935 (30). IR (KBr, cm^{-1}): 2547, ν(B−H).

2.5. Aerobic Decomposition of $Tp^{Ph,Me}Ni-O-2,6-^{i}Pr_2C_6H_3$ (1a): Identification and Quantification of Organic Coproducts. The mother liquor from the sample of decomposed $Tp^{Ph,Me}Ni-O-2,6-^{i}Pr_2C_6H_3$ (**1a**) (*vide supra*) was evaporated to give a yellow-orange amorphous residue. Naphthalene was added as an internal standard, and the solids were redissolved in dichloromethane (4.0 mL) and filtered through a plug of silica gel. The solution was injected into a Shimadzu GCMS-QP2010S instrument at 270 °C, with the column initially at 50 °C, and then the temperature was ramped upward at 10 °C/min for 5 min, 15 °C/min for 10 min, and 20 °C/min for 3 min and then held at 310 °C (Figures S24 and S25 of the Supporting Information). Peak assignments (except **U2**) were confirmed by comparison to the authentic standards described above (Figures S9−S22). Qualitatively similar results were observed by ^{1}H NMR spectroscopy of CD_2Cl_2 extracts (Figures S26−S29).

2.6. Aerobic Decomposition of $Tp^{Me,Me}Ni-O-2,6-^{i}Pr_2C_6H_3$ (1b): Isolation of $[Tp^{Me,Me}Ni]_2(\mu\text{-}CO_3)$ (3). A sample of **1b** (42 mg, 0.08 mmol) was dissolved in CH_2Cl_2 (10 mL) and reacted with O_2 as described for **1a** above. The solution changed color from orange to dark green within 3 h (Figure S35). Green crystals of $[Tp^{Me,Me}Ni]_2(\mu\text{-}CO_3)$ (**3**) were grown by diffusion of *n*-hexane (yield: 16 mg, 0.02 mmol, 51%). Spectra of **3** are shown in Figures S45−S48. Anal. Calcd (found) for $C_{31}H_{44}B_2N_{12}Ni_2O_3$, **3**: C, 48.24 (47.88); H, 5.75 (5.75); N, 21.78 (21.52). ^{1}H NMR (CD_2Cl_2, 293 K; δ, ppm): 43.4 (6H, 4-pz); 1.7 (18H, 3-Me); −4.7 (2H, B-*H*); −5.5 (18H, 5-Me). μ_{eff} = 2.22 μ_B ($CDCl_3$, 293 K). UV−vis−NIR (CH_2Cl_2;

λ_{max}, nm; ε, M^{-1} cm^{-1}): 412 (400); 657 (80); 839 (50). IR (KBr, cm^{-1}): 2504, ν(B−H); 1577, $\nu(CO_3)$.

2.7. Hydrolytic Decomposition of $Tp^{Ph,Me}$Ni−O-2,6-^{i}Pr$_2$C$_6$H$_3$ (1a): Isolation of [($Tp^{Ph,Me}$)$_2$Ni] (4). A sample of **1a** (31 mg, 0.04 mmol) was dissolved under argon in dichloromethane (8 mL). Degassed H_2O (30 μL, 1.7 mmol) was injected, and the dark green solution turned to a pale blue-green color within 15 min. The solvent was removed under vacuum, the residue was extracted with dichloromethane, and the extracts were filtered. Pale blue-green crystals of **4** were obtained by diffusion of *n*-hexane. Yield: 24 mg (0.02 mmol, 100%). Spectra of **4** are shown in Figures S57−S60. Anal. Calcd (found) for $C_{60}H_{56}B_2N_{12}Ni$, **4**: C, 70.27 (70.15); H, 5.50 (5.65); N, 16.39 (16.35). ^{1}H NMR ($CDCl_3$, 293 K; δ, ppm): 55.1 (3H, 4-pz); 7.3 (6H, 3-Ph); 5.9 (9H, 3-Ph); −1.7 (18H, 5-Me); −8.0 (1H, B-*H*). μ_{eff} = 3.16 μ_B ($CDCl_3$, 293 K). UV−vis−NIR (CH_2Cl_2; λ_{max}, nm; ε, M^{-1} cm^{-1}): 370 (sh, 15); 416 (10, sh); 603 (7.4); 762 (2.9); 992 (4.5). IR (KBr, cm^{-1}): 2549, ν(B−H).

2.8. DFT Calculations. A simplified TpNiOPh model was derived from our previous TpNiSPh models by replacement of sulfur with oxygen, adjustment of the resulting Ni−O and O−C_{ipso} bond lengths to experimental values, and geometry optimization.[59] Hypothetical O_2 adducts were modeled by manipulating the N−Ni−OAr and Ni−O−Ar angles within the mirror plane and inserting the oxygen atoms into the resulting gap. All geometry optimizations were restrained to C_s point symmetry. Spin-unrestricted calculations were performed using the Amsterdam Density Functional software package (version 2008.01, Scientific Computing and Modelling NV),[69,70] using the Vosko−Wilk−Nusair LDA functional,[71] the Becke−Perdew GGA correction,[72,73] and the Slater-type TZP orbital basis set available in the ADF library, with frozen atomic cores and default convergence criteria. A solvation model and relativistic correction were not applied.

2.9. X-ray Crystallography. Suitable crystals were placed onto the tips of 0.1 mm diameter glass capillaries and mounted on a Bruker APEX-II CCD diffractometer.[74] The data collection was carried out using Mo Kα radiation (graphite monochromator) with a frame time of 20−60 s and a detector distance of 6.0 cm. The data were corrected for absorption and decay (SADABS).[75] Final cell constants were calculated from strong reflections from the actual data collection after integration (SAINT).[76]

Structures were solved by direct methods and difference Fourier techniques using SHELXS-97 (Sheldrick, 1990) and SHELXL-97 (Sheldrick, 1997).[77] Space groups were determined on the basis of systematic absences and intensity statistics. All non-hydrogen atoms were refined with anisotropic displacement parameters. Hydrogen atoms were placed in ideal positions and refined as riding atoms with relative isotropic displacement parameters. Crystal and refinement information is summarized in Table 1 and additional comments specific to individual structure solutions are summarized below. Thermal ellipsoid plots are shown in Figures 1, 3, 4, and 7;[78] relevant bond lengths and angles are given in the captions.

For **1b**, the hydrogen atom on boron was located in a similar manner to the non-hydrogen atoms and refined isotropically. The dimeric structure of **2** sits on an inversion center, and only half of the molecule is unique. The diffraction data of **3** were initially indexed to a C-centered orthorhombic unit cell with twice the volume of the final monoclinic unit cell. XPREP suggested space group $C222_1$, which is rare, and no solution could be found in it. The reassigned monoclinic unit cell has nearly equivalent *a*- and *c*-axes, yet CHECKCIF and other routines found no additional symmetry. The crystal was twinned, and the twin element is a 180° rotation about [101]. A test was performed to determine the twin law. There are two twin components related by [0 0 1/0 1 0/1 0 0] in a ratio of 0.455:0.545. This implies the twins are enantiomorphs. The refinement yielded a Flack parameter of 0.00(2). The nickel atom of **4** is located on a special position (2-fold rotation axis), so that half of the molecule is the asymmetric unit. The hydrogen atom bonded to boron was located and refined with isotropic displacement parameters. The structure of **4** is isomorphous with the cobalt analogue.[79]

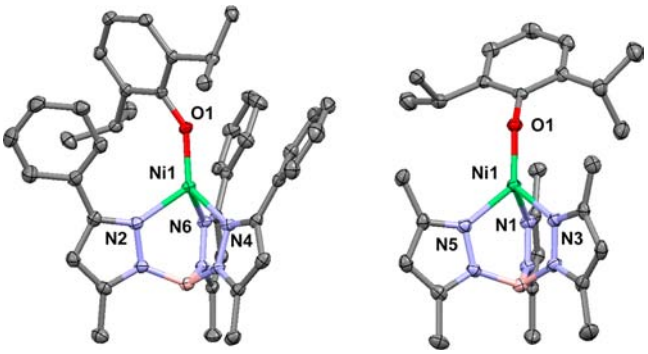

Figure 1. Thermal ellipsoid plots (50% probability) of $Tp^{Ph,Me}$Ni−O-2,6-^{i}Pr$_2$C$_6$H$_3$ (**1a**, left) and $Tp^{Me,Me}$Ni−O-2,6-^{i}Pr$_2$C$_6$H$_3$ (**1b**, right). Hydrogen atoms are omitted for clarity. Relevant bond lengths (Å) and angles (deg) for **1a**: Ni1−N2, 2.046(2); Ni1−N4, 2.017(1); Ni1−N6, 2.025(1); Ni1−O1, 1.821(1); N2−Ni1−N4, 91.52(6); N2−Ni1−N6, 95.53(6); N4−Ni1−N6, 88.63(6); N2−Ni1−O1, 121.91(5); N4−Ni1−O1, 130.14(6); N6−Ni1−O1, 119.72(5); Ni1−O1−C31, 147.8(1). For **1b**: Ni1−N1, 2.005(2); Ni1−N3, 1.982(2); Ni1−N5, 2.014(2); Ni1−O1, 1.841(2); N1−Ni1−N3, 91.71(9); N1−Ni1−N5, 91.37(9); N3−Ni1−N5, 90.09(9); N1−Ni1−O1, 118.99(9); N3−Ni1−O1, 124.41(9); N5−Ni1−O1, 129.92(9); Ni1−O1−C16, 138.9(2).

3.0. RESULTS

3.1. General Remarks. Photochemical generation of singlet ($^1\Delta_g$) dioxygen in the presence of 2,6-diisopropylphenol results in a one-electron redox reaction through net hydrogen atom abstraction to yield superoxide and phenoxyl radicals.[68] The latter decomposes by competitive dimerization and O_2 coupling to yield a mixture of 3,5,3′,5′-tetraisopropyl-4,4′-diphenoquinone and 2,6-diisopropyl-1,4-benzoquinone, respectively representing 2- and 4-electron oxidations per phenol precursor (Scheme 2). We hypothesized that substitution of the phenolic proton with paramagnetic [$Tp^{R,Me}$Ni(II)]$^+$ would provide the means to overcome the spin barrier of ground-state ($^3\Sigma_g^-$) O_2 and obtain analogous thermal reactivity.[18] Reduced O_2 species would then be captured for aromatic oxidation akin to the CAO active site, although the phenolate *ortho* sites are blocked by substituents. We accordingly prepared and characterized pseudotetrahedral $Tp^{R,Me}$Ni−OAr complexes (R = Ph, **1a**; Me, **1b**), which are thermally stable under inert atmosphere but decompose when exposed to O_2. Products consistent with phenoxyl radical formation were observed, as well as aromatic oxidation reactions, either on the supporting ligand of **1a** or on the phenolate ring of **1b**. However, 2,6-disubstituted phenolates will undergo free radical autoxidation to diphenoquinones under alkaline conditions,[80] and therefore hydrolyses of **1a,b** and subsequent oxidation reactions with O_2 and H_2O_2 were also examined.

3.2. Synthesis and Characterization of $Tp^{R,Me}$Ni−O-2,6-^{i}Pr$_2$C$_6$H$_3$ (1a,b). The phenolate complexes (R = Ph, **1a**; Me, **1b**) were obtained as crystalline solids following deprotonation of the phenol with sodium hydride and metatheses with known $Tp^{R,Me}$Ni−Cl precursor complexes.[65,66] Structures of **1a,b** were determined by X-ray diffraction (Figure 1). As expected, the N_3O ligand fields adopt pseudotetrahedral geometries that are nearly identical for both complexes. Constrained $Tp^{R,Me}$ ligand chelation yields average N−Ni−N angles of 92(3)° in **1a** and 91(1)° in **1b**, resulting in umbrella distortions with Ni−N bond vectors at respective angles of 123.9(3)° and 124.5(3)° from an ideal 3-fold axis. The

Scheme 2

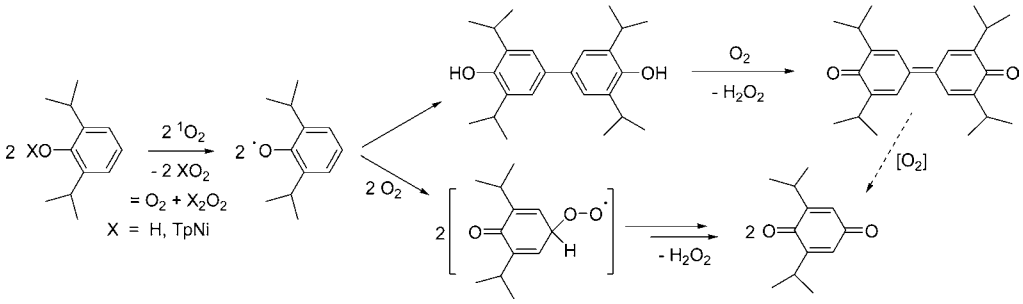

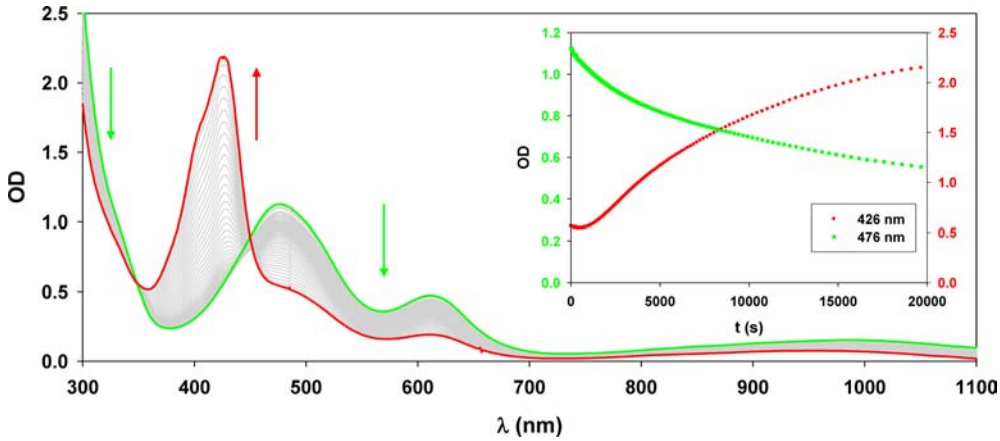

Figure 2. UV−vis−NIR spectra for decomposition of **1a** (0.61 mM) in CH_2Cl_2 under O_2 (306 K). The inset shows traces at 476 nm (green trace, left axis) and 426 nm (red trace, right axis), corresponding to the absorption maxima of **1a** and 3,5,3′,5′-tetraisopropyl-4,4′-diphenoquinone, respectively.

phenolate oxygen is then slightly displaced off this trigonal axis, with N−Ni−O angles ranging from 119.72(5)° to 130.14(6)° for **1a** and from 118.99(9)° to 129.92(9)° for **1b**, giving τ_4 values of 0.77 for **1a** and 0.75 for **1b**.[81] The Ni−OAr bond lengths are 1.821(1) and 1.841(2) Å, and the Ni−O−C_{ipso} bond angles are 147.8(1)° and 138.9(2)° in **1a**,**b**, respectively. The average Ni−N bond lengths of 2.03(2) and 2.00(2) Å in **1a**,**b** compare to values of 1.98(2) and 1.99(2) Å in the respective $Tp^{R,Me}$NiCl precursors.[66,82]

The spectroscopic data of **1a**,**b** are consistent with the solid-state structures. The IR spectra of **1a**,**b** exhibit ν(B−H) modes at 2543 and 2523 cm^{-1}, respectively (Figures S1−S4 of the Supporting Information), indicative of κ^3-$Tp^{R,Me}$ chelation.[83] The complexes exhibit intense green (**1a**) and orange (**1b**) colors, reflecting visible phenolate−Ni(II) LMCT bands, as well as weaker ligand field bands in the near-IR, with extinctions consistent with the noncentrosymmetric geometries (Figures S5 and S6). The LMCT bands are similar to those of the arylthiolate analogues, with somewhat attenuated extinctions.[58,59] The ligand field bands are similar to those of both the arylthiolate analogues and the chloride complex precursors, although small blue shifts in energies are evident in the following order: −SAr > −Cl > −OAr; $Tp^{Me,Me}$ ≥ $Tp^{Ph,Me}$.[58,59] In view of the low symmetry and lack of near-IR data, rigorous assignments of the ligand field bands of **1a**,**b** are not offered, although such analyses were reported previously for $Tp^{iPr,iPr}$Ni−SC_6F_5 and $Tp^{Me,Me}$Ni−Cl.[57,84] Magnetic susceptibilities in $CDCl_3$ solutions, determined by the Evans NMR method,[67] gave values of 2.72 and 3.09 μ_B at 293 K for **1a**,**b**, respectively, indicative of an orbitally nondegenerate paramagnetic ground state (i.e., μ_S = 2.83 μ_B for S = 1) and similar to the cases of both the chloride complex precursors and several arylthiolate analogues.[58,59] The ^{1}H NMR resonances of **1a**,**b** accordingly exhibit significant contact shifts, but the spectra were nonetheless consistent with the assigned formulations (Figures S7, S8). As with the arylthiolate analogues,[58,59] spin delocalization by π-polarization leads to pronounced upfield shifting of the phenolate *para* protons, with the *meta* and isopropyl methine protons shifted downfield, and the isopropyl methyl resonance nearer to the diamagnetic limit. The pyrazole resonances of the supporting Tp ligands are unremarkable. However, the borohydride resonances of **1a**,**b** both exhibit pronounced upfield shifts (−20 and −19 ppm at 293 K, respectively) compared to those of the chloride complex precursors (−14 and −13 ppm, respectively) and several arylthiolate analogues (typically −10 to −11 ppm),[58,59] reflecting the trend in the ligand field bands. All three pyrazoles, as well as both sides of the phenolate rings, are spectroscopically equivalent in the ^{1}H NMR spectra of **1a**,**b**, indicative of fluxionality in solution.

3.3. Reactivity: Oxygenation of 1a,b. The phenolate complex **1a** was indefinitely stable in a dilute solution of dry, anaerobic CH_2Cl_2 (Figure S23). However, rapid saturation of the solution of **1a** with O_2 resulted in monotonic bleaching of the absorption bands ($t_{1/2}$ ≈ 2 h at 306 K; Figure 2), coincident with growth of an intense band at 426 nm, assigned to 3,5,3′,5′-tetraisopropyl-4,4′-diphenoquinone (0.05 equiv, 10 mol %).[68] The induction period apparent in growth of this band reflects bleaching of coincident CT absorption of **1a** (Figure 2 inset), and presumably the initial accumulation of the dihydroquinone intermediate (Scheme 2), which disrupts the isosbestic points. GC-MS analysis of a decomposed aerobic solution with added

dx.doi.org/10.1021/ic300551z | Inorg. Chem. 2012, 51, 7257−7270

naphthalene as an internal standard (**A**; t = 8.0 m, m/z = 128; Figures S24 and S25) revealed a small fraction of unmodified 2,6-diisopropylphenol (**B**; 9.6 m, m/z = 178; 14 mol %), as well as 2,6-diisopropyl-1,4-benzoquinone (**C**; 10.1 m, m/z = 192; 15 mol %) and overlapping 3,5,3′,5′-tetraisopropyl-4,4′-diphenoquinone (**E**; 17.80 m, m/z = 354!) and 3,5,3′,5′-tetraisopropyl-4,4′-diphenodihydroquinone (**F**; 17.83 m, m/z = 354; 46 mol % combined with **E**); the combined yield of phenol equivalents was 76 mol %. A peak corresponding to 2,6-diisopropyl-1,4-benzodihydroquinone (**D**; 12.3 m, m/z = 194) was not observed. Two additional unknown peaks were assigned as 3-phenyl-5-methylpyrazole (**U1**; 12.4 m, m/z = 158, 0.20 equiv) and 4-hydroxy-3,5-diisopropylphenyl-2,6-diisopropyl ether (**U2**; 15.6 m, m/z = 354), the product of head-to-tail phenoxy radical coupling. The assignments of **U1** (data not shown) and **B**−**F** (Figures S18−S22) were confirmed by comparison to authentic standards. Qualitatively similar results were observed by ^{1}H NMR spectroscopy of CD_2Cl_2 extracts (Figures S26−S29), except the diphenodihydroquinone was oxidized. Thus, the organic product mixture is analogous to that previously reported for oxidation of phenol by singlet oxygen,[68] consistent with formation of phenoxyl radical and obligating concomitant generation of reduced oxygen species (Scheme 2). Further evidence for a reactive oxygen intermediate was obtained from isolation of product complex **2**, with an oxidized ligand.

Complex **2**, obtained as pale green crystals in 53% yield, was characterized by X-ray crystallography (Figure 3). A dimeric structure occupies a crystallographic inversion center, so only half of the molecule is unique. Both nickel atoms are ligated with a modified $Tp^{Ph,Me}$ ligand resulting from C−H bond hydroxylation at the *ortho* position of one 3-phenyl substituent (i.e., $Tp^{Ph,Me*}$), a two-electron oxidation. The planar Ni(II)$_2$(OR)$_2$ core adopts a Ni···Ni separation of 3.1207(5) Å and an O···O separation of 2.587(3) Å, with internal O−Ni−O and Ni−O−Ni angles of 79.32(8)° and 100.68(8)°, respectively. The Ni1−O1 bond length within the κ^4-chelate is longer than the bridging Ni1−O1′ bond length, 2.043(2) vs 2.010(2) Å. These core metrical parameters are similar to those of previously characterized [TpNi(μ-OH)]$_2$ complexes.[32−34] The Ni1−O1−C10$_{ipso}$ and Ni1−O1′−C10′$_{ipso}$ angles are 130.0(2)° and 126.8(2)°, respectively. The modified dianionic tetradentate ligand binds Ni(II) in a distorted trigonal pyramidal geometry (τ_4 = 0.65)[81] with an axial N2 donor atom on the same tripodal arm as the equatorial phenolate (i.e., O1). The Ni1−N2 bond is shorter than the Ni1−N4 and Ni1−N6 bonds, 2.000(2) vs 2.054(2) and 2.134(2) Å, respectively. The open axial site is filled by the opposing phenolate oxygen (i.e., O1′) in the assembled dimer, giving an N2−Ni1−O1′ angle of 164.81(8)°. However, the overall N_3O_2 ligand field is best described as a distorted square pyramid (τ = 0.32)[85] with an axial N4 donor. The central Ni_2O_2 core is canted 12.6° relative to the axial B−N1−N2−Ni1−O1′ least-squares planes, with the two tripodal ligands disposed over opposite faces, which results in diverging N4−Ni1−O1 and N6−Ni1−O1 bond angles of 122.82(8)° and 145.73(8)°.

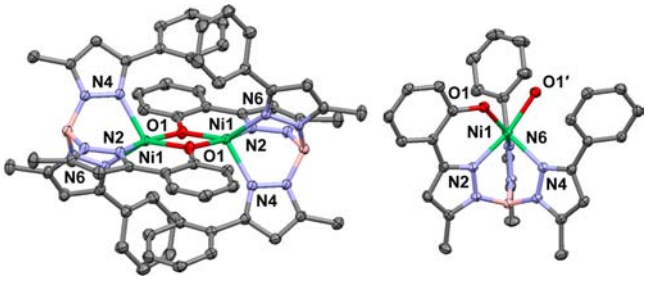

Figure 3. Thermal ellipsoid plot (30% probability) for dimeric [($Tp^{Ph,Me*}$)Ni]$_2$ (**2**, left) and the monomeric asymmetric unit (right). Hydrogen atoms are omitted for clarity. Relevant bond lengths (Å) and angles (deg): Ni1−N2, 2.000(2); Ni1−N4, 2.054(2); Ni1−N6, 2.134(2); Ni1−O1, 2.043(2); Ni1−O1′, 2.010(2); Ni1···Ni1′, 3.1207(5); O1···O1′, 2.587(3); N2−Ni1−N4, 89.78(8); N2−Ni1−N6, 89.40(8); N4−Ni1−N6, 90.97(8); N2−Ni1−O1, 85.55(8); N4−Ni1−O1, 122.82(8); N6−Ni1−O1, 145.73(8); N2−Ni1−O1′, 164.81(8); N4−Ni1−O1′, 99.54(8); N6−Ni1−O1′, 102.32(7); O1−Ni1−O1′, 79.32(8); Ni1−O1−Ni1′, 100.68(8); Ni1−O1−C10, 130.0(2); Ni1−O1′−C10′, 126.8(2).

Six-coordinate Fe(III) complexes of $Tp^{Ph,Me*}$ and $Tp^{Ph,Ph*}$ ligands were obtained previously,[86,87] by oxidation with O_2 or H_2O_2, and resonance Raman spectroscopy of the latter derivative revealed vibrational modes of the *ortho*-phenolate ring.[87] The solid-state IR spectrum of **2** contains several analogous bands, as well as a single ν(B−H) mode at 2547 cm^{-1}, consistent with κ^3-pyrazole ligation and ideal C_{2h} point symmetry (Figures S30 and 31). The UV−vis−NIR spectrum of **2** in CH_2Cl_2 contains intense bands at 306, 317, and 420 nm, which can be assigned as LMCT transitions arising from the installed phenolate moieties,[41,42,88] as well as weaker ligand field bands at longer wavelengths (Figure S32). The band at 420 nm exhibits a reversible, temperature-dependent red-shift (Figure S33), suggesting a solution-phase equilibrium. Notwithstanding antiferromagnetic coupling of Ni(II) ions in the dimeric complex (μ_{eff} = 2.42 μ_B in $CDCl_3$), the ^{1}H NMR spectrum in $CDCl_3$ exhibits signals over a significant range of chemical shifts comparable to those for **1a**,**b** (ca. −30 to 80 ppm, Figure S34). Thus, dissociation of **2** to monomeric ($Tp^{Ph,Me*}$)Ni in solution is suggested. However, further analysis was complicated by the low solubility of the isolated crystalline solids, and the NMR spectrum was not fully assigned.

Aerobic decomposition of **1b** appeared similar to that of **1a** by UV−vis−NIR spectroscopy (Figure S35), albeit at a ca. 10-fold faster rate (at 293 K vs 303 K) and with a diminished yield of diphenoquinone (ca. 6 mol %). A slight increase in optical density broadly centered near 642 nm likely reflects accumulation of [$Tp^{Me,Me}$Ni(μ-OH)]$_2$.[34] As for decomposition of **1a**, GC-MS analysis of the organic products revealed formation of diphenoquinone with traces of benzoquinone and unmodified phenol (Figures S36 and S37), and this was confirmed by ^{1}H NMR spectroscopy (Figures S38 and S39). However, two significant unknown species **U3** and **U4** were also observed. The unknown components were isolated by chromatography on silica and characterized by ^{1}H NMR spectroscopy in CD_2Cl_2 solution (Figures S40−S44). The data for the major product **U4** unambiguously indicate loss of ring aromaticity and symmetry, as the three ring protons shifted to 6.77 (1H, d, J = 4.3 Hz), 3.72 (1H, d, J = 4.0 Hz), and 3.59 ppm (1H, dd). A fourth proton resonance, presumably arising from phenol tautomerization, appeared at 3.67 ppm (1H, s). Moreover, the isopropyl groups also lost equivalence, exhibiting distinct methine septets at 2.80 and 1.88 ppm, each coupled to pairs of diastereotopic methyl signals. This spectrum appears to be consistent with assignment of **U4** as 3,4-dihydro-3,4-dihydroxy-2,6-diisopropylcyclohex-5-enone, which apparently has not been reported previously. This product is consistent with aromatic dihydroxylation of phenol by addition of H_2O_2 or its equivalent across *meta* and *para* ring positions, a two-

electron oxidation distinct from the aromatic C−H bond hydroxylation that yields **2**. The spectrum of the minor product **U3** was not fully resolved, and a structure was not assigned.

Also isolated from a solution of aerobically decomposed **1b** was a dimeric carbonato-bridged complex with unmodified scorpionate ligands, $[Tp^{Me,Me}Ni]_2(\mu\text{-}CO_3)$ (**3**), as pale green crystals in 51% yield. This complex presumably arises from the previously reported $[Tp^{Me,Me}Ni(\mu\text{-}OH)]_2$ by CO_2 capture during workup under air.[34,89] Complex **3** was characterized by X-ray diffraction (Figure 4). The nickel atoms of **3** lie on the same side of the carbonato ligand plane, in contrast to the previously reported Tp^{iPr2} analogue,[89] and are more trigonally distorted (τ = 0.27 and 0.20 for Ni1 and Ni2, respectively, vs 0.16 and 0.14). The Ni−O bonds to the bridging oxygen are longer than those to the unshared oxygens in **3**, 2.104(7) and 2.144(7) Å vs 2.021(7) and 1.963(6) Å, similar to a Tp^{Cy}-supported dimer,[90] but reversed from the Tp^{iPr2}-supported complex.[89] The bridging Ni−O−Ni angle is correspondingly decreased, from 178.0(1)° in the latter[89] to 169.7(4)° in **3**. Within the carbonato ligand, the carbon−oxygen bond to the bridging oxygen in **3** is longer than those to the two terminal oxygens, 1.37(1) Å vs 1.27(1) and 1.22(1) Å. The IR spectrum of **3** contains a band at 1577 cm^{-1} assigned to the carbonato ligand (Figures S45 and S46), compared to 1568 and 1581 cm^{-1} in the respective Tp^{iPr2}- and Tp^{Cy}-supported analogues.[89,90] The UV−visible−NIR (Figure S47) and ^1H NMR spectra of **3** (Figure S48) are also consistent with these prior results,[89] with the latter exhibiting attenuated contact shifting due to antiferromagnetic coupling through the carbonato bridge (μ_{eff} = 2.22 μ_B).

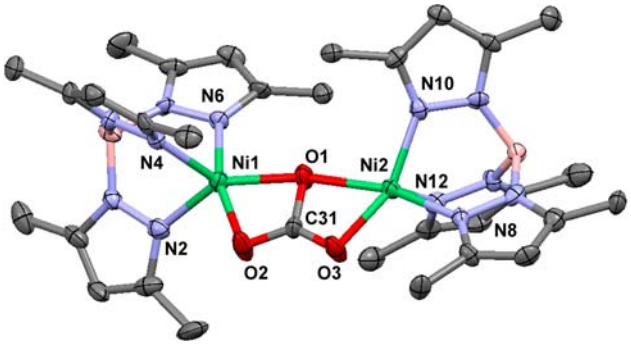

Figure 4. Thermal ellipsoid plot (30% probability) of $[Tp^{Me,Me}Ni]_2(\mu\text{-}CO_3)$ (**3**). Hydrogen atoms are omitted for clarity. Relevant bond lengths (Å) and angles (deg): Ni1−N2, 2.016(8); Ni1−N4, 2.009(7); Ni1−N6, 2.021(6); Ni1−O1, 2.104(7); Ni1−O2, 2.021(7); Ni2−N8, 2.054(6); Ni2−N10, 1.955(8); Ni2−N12, 2.041(8); Ni2−O1, 2.144(7); Ni2−O3, 1.963(6); C31−O1, 1.37(1); C31−O2, 1.27(1); C31−O3, 1.22(1); N2−Ni1−N4, 90.6(3); N2−Ni1−N6, 91.8(3); Ni4−Ni1−N6, 91.6(3); N2−Ni1−O1, 146.9(3); N2−Ni1−O2, 95.0(3); N4−Ni1−O1, 118.3(3); N4−Ni1−O2, 103.9(3); N6−Ni1−O1, 102.3(2); N6−Ni1−O2, 162.9(3); O1−Ni1−O2, 64.2(2); O1−C31−O2, 112.5(8); O1−C31−O3, 116.1(8); O2−C31−O3, 131.0(8); N8−Ni2−N10, 90.5(3); N8−Ni2−N12, 90.9(3); Ni10−Ni2−N12, 92.4(3); N8−Ni2−O1, 161.1(2); N8−Ni2−O3, 97.5(3); N10−Ni2−O1, 102.2(3); N10−Ni2−O3, 149.0(3); N12−Ni2−O1, 102.3(3); N12−Ni1−O3, 117.2(3); O1−Ni2−O3, 64.5(3); Ni1−O1−Ni2, 169.7(4).

3.4. Reactivity: Hydrolyses of 1a,b and Subsequent Oxidations with O_2 and H_2O_2. Given the basicity of the phenolate ligands, complexes **1a,b** are susceptible to hydrolysis. We cannot exclude the possibility that the observed decompositions already described are rate-limiting hydrolyses due to introduction of H_2O. Rapid autoxidation of free phenol might then yield H_2O_2, and precedent exists for peroxide activation and oxidative chemistry at TpNi(II) centers.[30−34]

Therefore, hydrolysis reactions were carried out in which excess H_2O was deliberately added to solutions of **1a** and **1b** in CH_2Cl_2. This resulted in simple bleaching of the LMCT bands in both cases (Figures 5 and S49). A UV−vis−NIR spectrum of the hydrolyzed solution of **1b** at equilibrium was consistent with a mixture of previously reported $[Tp^{Me,Me}Ni(\mu\text{-}OH)]_2$ (70 mol % based on reported extinctions)[34] and an unknown minor species that exhibits ligand field bands typical of a pseudotetrahedral TpNi−X complex (Figure S49). Attempts to isolate the immediate product complex from hydrolysis of **1a**, putatively the unknown monomeric analogue $[Tp^{Ph,Me}Ni-OH]$, instead gave the previously unreported and spectroscopically distinct sandwich complex $[(Tp^{Ph,Me})_2Ni]$ (**4**) as pale blue-green crystals in quantitative yield (i.e., 0.5 equiv). Subsequent addition of excess H_2O_2 to the solution of hydrolyzed **1a** rapidly generated complex **2** in quantitative spectroscopic yield (Figure 5), as confirmed by ^1H NMR (Figure S50) and FTIR (Figures S51 and S52) spectroscopy, without accumulation of diphenoquinone. Treatment of **4** with excess H_2O_2 also resulted in conversion to **2**, albeit much more slowly (Figure S53).

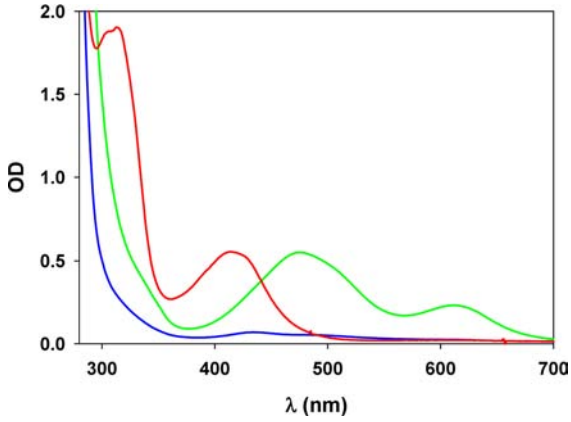

Figure 5. UV−vis spectra demonstrating reaction of **1a** (0.30 mM, green) with added H_2O (270 mM) to form a hydrolyzed intermediate (blue) that reacts rapidly with H_2O_2 (67 mM) to form **2** (red).

Notwithstanding the above results, phenol oxidation following hydrolyses of **1a,b** and O_2 addition was slow and inefficient (Figures 6 and S54). Exposure of hydrolyzed **1a,b** to O_2 resulted in relatively slow generation of weak absorption bands at 426 nm, consistent with diminished accumulation of diphenoquinone (≤3.0 mol %) and **2** (Figures 6 and S54, insets). GC-MS analysis of the product mixtures after standing 24 h demonstrated that the balance of organic product was unmodified 2,6-diisopropylphenol (Figures S55 and S56). Autoxidation of free phenol is plausible, but accumulation of diphenoquinone, and hence reduction of O_2, is faster and more extensive without added H_2O (Figures 2 and S35). The excess H_2O, which is necessary to effect prompt hydrolyses of **1a,b**, might act as a significant inhibitor of phenol autoxidation, perhaps by compromising the efficacy of the $[Tp^{R,Me}Ni-OH]$ coproduct as a base catalyst. Otherwise, it seems necessary to ascribe the difference in O_2 chemistry without added H_2O to oxidation of intact **1a,b**.

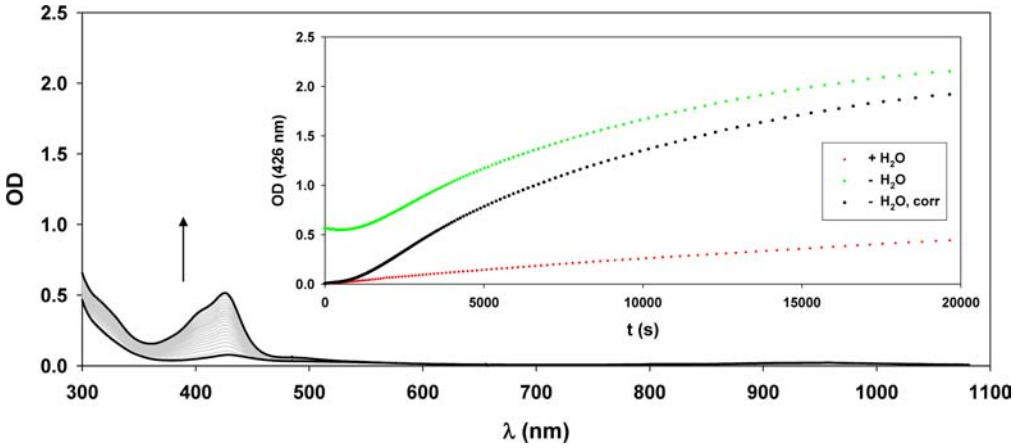

Figure 6. UV−vis−NIR absorption vs time (Δt = 1000 s) following addition of O_2 to a hydrolyzed solution of **1a** (0.44 mM in CH_2Cl_2, 306 K). The inset shows a trace at 426 nm (red), corresponding to accumulation of 3,5,3′,5′-tetraisopropyl-4,4′-diphenoquinone, and compared to the data shown in Figure 2 for O_2 addition to intact **1a** (green) and corrected for absorption of **1a** (black).

A crystal structure of complex **4** confirmed the sandwich structure, $[(Tp^{Ph,Me})_2Ni]$ (Figure 7). Despite the steric bulk of opposing 3-phenyl substituents, the nickel ion resides in a pseudo-octahedral, ideally D_{3d} N_6 ligand field afforded by κ^3-*fac* ligation of the two ligands. The average Ni−N bond length of 2.18(4) Å and nonbonded Ni···B distances of 3.057(2) Å can be compared to other reported sandwich structures: $(Tp^{4Bo})_2Ni$, 2.087(4) and 3.161(6) Å;[91] $(Tp)_2Ni$, 2.093(7) and 3.165(3) Å;[92] $(Tp^{Me})_2Ni$, molecule 1, 2.11(2) and 3.140(7) Å;[93] $(Tp^{Me})_2Ni$, molecule 2, 2.096(6) and 3.16(1) Å;[93] $(Tp^{Me,Cl,Me})_2Ni$, molecule 1, 2.10(1) and 3.13(1) Å;[94] $(Tp^{Me,Cl,Me})_2Ni$, molecule 2, 2.11(1) and 3.143(7) Å;[94] $(Tp^{Np})_2Ni$, 2.12(1) and 3.089(6) Å;[95] $(Tp^{Me,Me})_2Ni$, 2.13(2) and 3.055(6) Å;[96] $(Tp^{CO2Et,Me})_2Ni$, 2.14(6) and 3.105(6) Å;[97] $(Tp^{3py})_2Ni$, 2.15(7) and 3.078(2) Å;[98] $(Tp^{4bz})_2Ni$, 2.18(5) and 3.115(7) Å;[99] (4Bo, 4,5-fused benzo ring {i.e., indazolyl vs pyrazolyl}; Np, neopentyl, $CH_2C(CH_3)_3$; 3-py, *meta*-C_5H_4N; 4bz, *para*-C_6H_4−C≡N). An inverse and counterintuitive trend in the Ni−N and Ni···B distances can be inferred from these data, in which increased steric bulk of 3- and 5-pyrazole substituents favors longer Ni−N bonds within a more compact sandwich. The structure of **4** represents a new extreme, which is accommodated by significant B−N−N−Ni torsion angles in the pyrazole ring chelation, 15.2(1)−19.5(1)°. The intraligand *cis*-N−Ni−N bond angles remain close to right angles, 89.17(4)−91.48(4)°, but the interligand angles diverge, 82.71(4)−97.25(4)°, and the *trans* angles depart from linearity, 169.84(4)−171.31(6)°. The Ni−N5 bond lengths of 2.226(1) Å, disposed *trans* along one axis, are elongated compared to the orthogonal Ni−N1 and Ni−N3 bond lengths, 2.149(1) and 2.157(1) Å, respectively. The crystal lattice of **4** is isomorphous with that of the $(Tp^{Ph,Me})_2Co$ analogue, which exhibits a nearly identical structure with an average Co−N bond length of 2.21(5) Å and Co···B distances of 3.10(1) Å.[79]

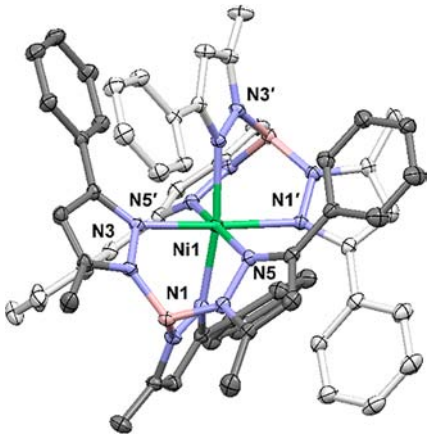

Figure 7. Thermal ellipsoid plot (30% probability) of $[(Tp^{Ph,Me})_2Ni]$ (**4**). For clarity, hydrogen atoms are omitted and the carbon atoms of opposing ligands are differentially shaded. Relevant bond lengths (Å) and angles (deg): Ni1−N1, 2.149(1); Ni1−N3, 2.157(1); Ni1−N5, 2.226(1); N1−Ni1−N3, 89.96(4); N1−Ni1−N5, 91.48(4); N3−Ni1−N5, 89.17(4); N1−Ni1−N1′, 96.32(6); N1−Ni1−N3′, 169.84(4); N1−Ni1−N5′, 82.71(4); N3−Ni1−N3′, 85.00(6); N3−Ni1−N5′, 97.25(4); N5−Ni1−N5′, 171.31(6), where the prime symbol denotes a nitrogen atom on the opposing ligand.

Spectral data of **4** are consistent with the sandwich structure. The IR spectrum of **4** contains a single ν_{as}(B−H) mode at 2549 cm^{-1} (A_{2u} under D_{3d} symmetry), indicative of dual κ^3-$Tp^{Ph,Me}$ ligation (Figures S57 and S58). The electronic spectrum of **4** in CH_2Cl_2 solution is typical of a pseudo-octahedral Tp_2Ni sandwich (Figure S59).[91,100] Spin-allowed ligand field transitions were observed at 990 ($^3A_{2g} \rightarrow {}^3T_{2g}$) and 603 nm ($^3A_{2g} \rightarrow {}^3T_{1g}$), and a spin-forbidden band ($^3A_{2g} \rightarrow {}^1E_g$) was observed at 762 nm (i.e., Δ_O = 10,100 cm^{-1}; B = 770 cm^{-1}). The third spin-allowed band ($^3A_{2g} \rightarrow {}^3T_{1g}\{P\}$) was obscured by tailing of stronger UV bands. Spectra of Tp_2Ni and $(Tp^{4Bo})_2Ni$ are blue-shifted, Δ_O = 12,000 and 12,890 cm^{-1}, respectively,[91,100] consistent with their shorter Ni−N bonds (*vide supra*).[91,92] The solution magnetic susceptibility of **4** (3.16 μ_B) is consistent with an ideal $^3A_{2g}$ ground state.[100] The ^{1}H NMR spectrum of **4** (Figure S60) exhibited equivalence of all pyrazoles, reflecting ideal 2- and 3-fold symmetry of the complex. Notwithstanding the steric hindrance evident in the structure, both edges of the 3-phenyl substituents also exhibit equivalence, consistent with rotation.

3.5. DFT Calculations. Oxidation of intact phenolate complexes with O_2 was suggested as a reaction mechanism leading to phenoxyl radical formation, but complex intermediates were not observed during aerobic decompositions of **1a**,**b**. Therefore, geometric and electronic models were sought for hypothetical inner-sphere O_2 adducts. Spin-unrestricted DFT calculations were performed first on a simplified TpNi−

OPh model (Figure 8A), related to the crystal structure of **1a**,**b** by replacement of scorpionate and phenolate ligand substituents with hydrogen. The O_2 adducts [TpNi(OPh)(O_2)] (Figure 8B−D) and [TpNi(O_2)] (Figure 8E−I) were modeled in turn, with the latter reflecting loss of phenoxyl radical subsequent to O_2 ligation. To simplify the computations and their interpretation, geometry optimizations were constrained to C_s symmetry in all cases. The calculated geometric parameters are summarized and compared (Table 2), and noteworthy features of the electronic structures are discussed below.

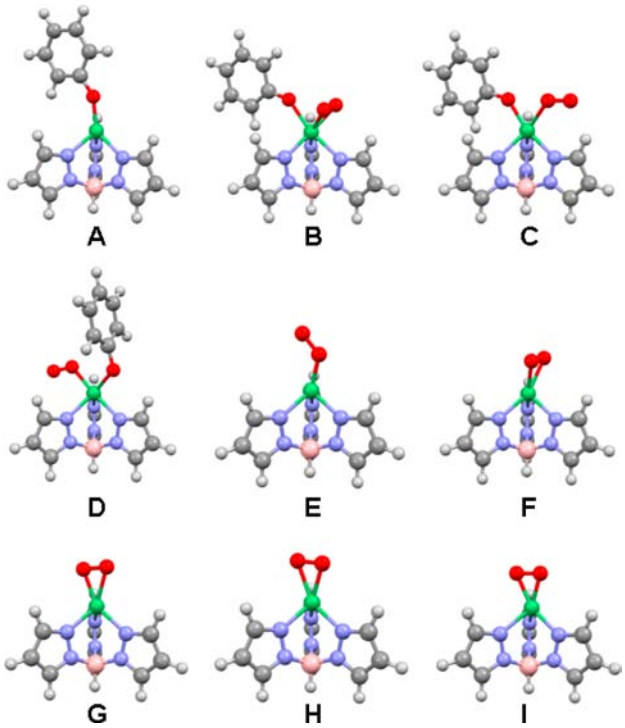

Figure 8. Optimized geometries of C_s-symmetric computational models of TpNiOPh (A), TpNiOPh(O_2) (B−D), and TpNiO_2 (E−I).

Geometry optimization of TpNiOPh yielded a sawhorse configuration comparable to the experimental structure of **1b** (Table 2, Figure 8A and Figure S61), with one large axial N−Ni−O bond angle of 134° and two smaller N−Ni−O bond angles of 121° (τ_4 = 0.74). The average Ni−N bond length was 2.05(1) Å, the Ni−OPh bond length was 1.84 Å, and the Ni−O−C_{ipso} bond angle was 149°; comparable values in **1b** are 2.00(2) Å, 1.841(2) Å, and 138.9(2)°, respectively. Frontier orbitals of interest included the five atomic d orbitals on nickel, as well as the in-plane and out-of-plane phenolate oxygen donor orbitals (i.e., β-spin orbitals 21a″ and 37a′, respectively), which were separated by 1.8 eV (Figure 9).[52] The electronic structure of TpNiOPh was similar to prior calculations on the arylthiolate analogues, except the relatively upright conformation of the phenolate disposes the ligand for π overlap of both donor orbitals, in contrast to the pseudo-σ interaction of bent arylthiolates.[57,59] Consistent with the imposed spin state (S = 1), the two lowest unfilled orbitals were β-spin (41a′ and 22a″), composed predominantly of atomic d orbitals on nickel (69% and 62%, respectively) and exhibiting σ^* interactions with the pyrazole N2 donor atoms and π^* interaction with the phenolate. The remaining β-spin Ni d orbitals (40a′, 39a′, and 20a″) were stabilized by an average of 1.8 eV and were filled, as were all five α-spin analogues. The α-spin HOMO−LUMO gap was 3.6 eV, and the latter was comprised entirely of pyrazole π^* interactions (not shown). The α- and β-spin HOMOs, presumably the redox-active orbitals in a one-electron oxidation, both exhibited major contributions from the out-of-plane phenolate π donor orbital.

After benchmarking the TpNiOAr model against the experimental data for **1a**,**b**, we calculated possible structures for a hypothetical O_2 adduct, [TpNi(OPh)(O_2)] (Figure 8B−D). Ordinary unrestricted calculations were performed, without consideration for effects of magnetic coupling between spins localized on nickel and the O_2 ligand. Four conformations are possible under C_s symmetry, with the phenolate ligand displaced *cis* or *trans* with respect to the axial pyrazole (defined as occupying the mirror plane) and O_2 introduced either end-on or side-on into the opened coordination site. Calculations with imposed low-spin (S = 0) states failed to converge, while high-spin (S = 2) states converged by dissociation of O_2 and return of the TpNiOPh fragment toward its previously described structure. In contrast, computations with intermediate spin (S = 1) converged in three of the four cases (Figure 8B−D), failing only for a trigonal prismatic geometry with an equatorial phenolate and side-on O_2. Of the three other models, the unique octahedral conformation with side-on O_2 and an axial phenolate (Figure 8B) was predicted to exhibit significant elongations of the Ni−OAr and *trans* Ni−N bonds along an axial vector (Table 2), suggesting Jahn−Teller

Table 2. Calculated Bond Lengths from Computational Models

model	structure[a]	S	O−O (Å)	Ni−O_2 (Å)[b]	Ni−OPh (Å)	Ni−N_{ax} (Å)[b]	Ni−N_{eq} (Å)[b]	relative energy (eV)
TpNiOPh + O_2	A	1 ± 1	1.23	∞	1.84	2.05	2.06	0.00
TpNiOPh(O_2)	B	1	1.33	1.94	2.11	2.14	1.99	+0.05
TpNiOPh(O_2)	C	1	1.28	2.09	1.91	2.02	2.09	+0.18
TpNiOPh(O_2)	D	1	1.28	1.91	1.89	2.06	2.06	−0.30
TpNiO_2 + PhO•	E	$^3/_2 \pm {}^1/_2$	1.31	1.87	∞	2.01	2.06	+0.98
TpNiO_2 + PhO•	F	$^3/_2 \pm {}^1/_2$	1.35	2.04	∞	2.03	2.07	+0.69
TpNiO_2 + PhO•	G	$^3/_2 \pm {}^1/_2$	1.34	1.99 (ax) 2.11 (eq)	∞	2.08	2.04	+0.73
TpNiO_2 + PhO•	H	$^1/_2 \pm {}^1/_2$	1.35	2.10 (ax) 2.01 (eq)	∞	2.06	2.03	+0.90
TpNiO_2 + PhO•	I	$^1/_2 \pm {}^1/_2$	1.37	1.89 (ax) 1.84 (eq)	∞	1.96	2.08	+0.46

[a]Figure 8. [b]Axial positions defined as pyrazole occupying the mirror plane and trans coordination site.

dx.doi.org/10.1021/ic300551z | Inorg. Chem. 2012, 51, 7257−7270

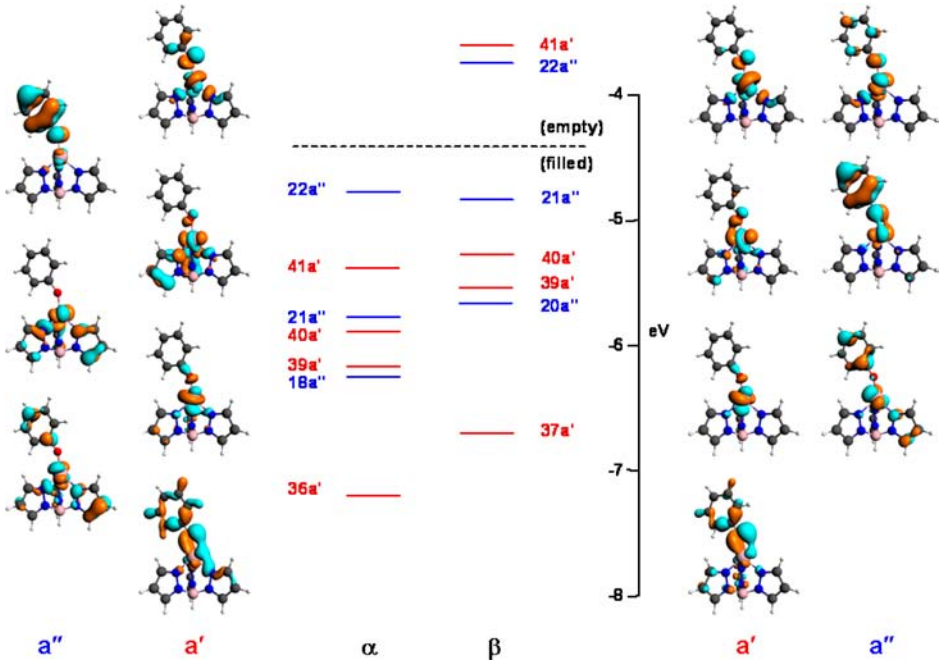

Figure 9. Relevant spin-unrestricted frontier molecular orbitals in the C_s-symmetric TpNiOPh computational model (Figure 8A), circumscribing five nickel d orbitals and the in-plane and out-of-plane phenolate donor orbitals. Red and blue orbitals and labels respectively signify symmetry (a′) and antisymmetry (a″) with respect to the mirror plane.

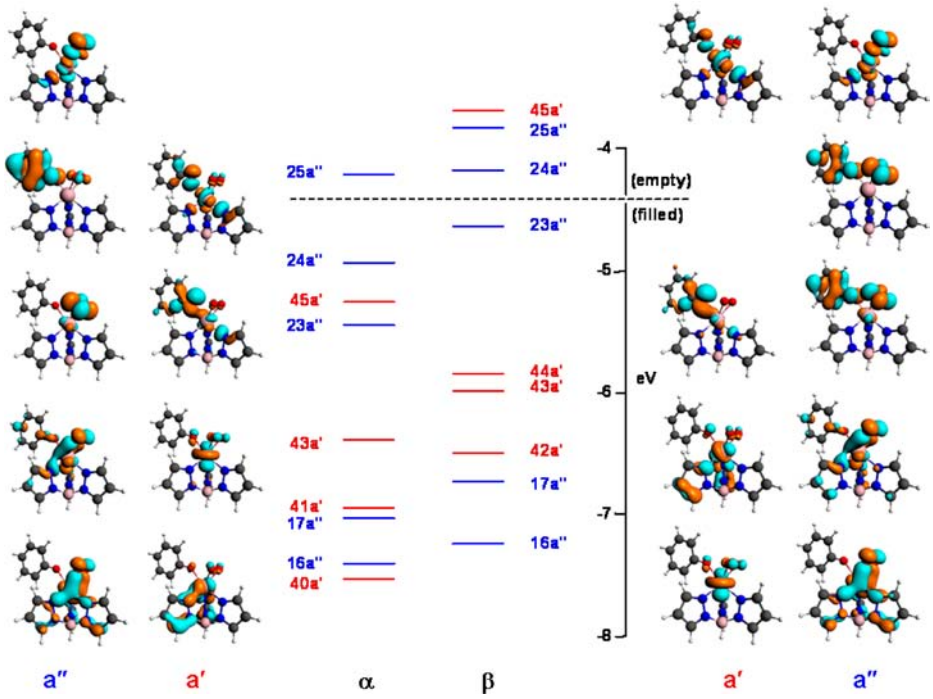

Figure 10. Relevant spin-unrestricted frontier molecular orbitals in a C_s-symmetric TpNiOPh(O_2) computational model (Figure 8B), circumscribing five nickel d orbitals, the two phenolate donor orbitals, and two O_2 π^* orbitals. Red and blue orbitals and labels respectively signify symmetry (a′) and antisymmetry (a″) with respect to the mirror plane.

distortion of a low-spin Ni(III) ion (d^7, $S = {}^1/_2$). A relatively long O−O bond was also predicted (Table 2), presumably facilitated by the side-on coordination. Four unoccupied orbitals were found at low energy (Figure 10): a pair of α- and β-spin σ^* orbitals (25a″) delocalized over the NiO_2 core; one β-spin orbital (45a′) consisting predominantly of the axially oriented dσ^* orbital on nickel; and a third β-spin hole (24a″) delocalized over both the O_2 and OPh ligands. The nature of the latter hole may facilitate phenoxide/superoxo and phenoxyl/peroxide valence isomerism. Taken as a whole, the octahedral conformation seems poised for facile homolysis of phenoxyl radical. The end-on conformations (Figure 8C and D) exhibited analogous electronic structures (Figures S62 and S63), notwithstanding their trigonal bipyramidal geometries, but the predicted O−O and Ni−OAr bond lengths were shorter. The end-on conformations may be disposed toward

intramolecular coupling of superoxo and phenoxo moieties,[51] perhaps constituting an origin for divergent aromatic oxidation pathways.

Loss of phenoxyl radical from the O_2 adduct would generate [TpNiO_2], and calculations were performed on three limiting conformations, end-on (pseudotetrahedral) and side-on (trigonal bipyramidal or square pyramidal), in both quartet ($S = {}^3/_2$, Figure 8E−G) and doublet states ($S = {}^1/_2$, Figure 8H−I). Assignment of oxidation states was complicated by the high degree of NiO_2 covalency, but calculated O−O bond lengths in the high-spin structures were typically consistent with those of superoxo ligands (Table 2). Accordingly, three vacant β-spin orbitals were found at low energy for the high-spin side-on models, two predominantly nickel-centered dσ* orbitals and one O_2-centered π* orbital. However, these orbitals exhibited decreased nickel d character in the end-on conformation, suggesting a shift toward univalent nickel (Figures S64−S66). The low-spin calculations were more opaque. The initially end-on model converged to a trigonal bipyramidal geometry that appears to enforce antiferromagnetic coupling in a superoxo-Ni(II) valence state (Figure S67), while an initially trigonal bipyramidal model converged with significantly contracted bond lengths, plausibly interpreted as peroxo−Ni(III) (Figure S68). The square pyramidal conformation failed to converge. Several Ni−O_2 adducts exhibiting low-spin EPR signals were recently reported, and DFT calculations supported similarly divergent experimental assignments of ground states, depending on the supporting ligand.[19−21,23,25,26]

4.0. DISCUSSION

Inspired by the dioxygenase activity of nickel-substituted apo-CAO,[54,55] we prepared and characterized the pseudotetrahedral phenolate complexes $Tp^{R,Me}$Ni−OAr (R = Ph, **1a**; Me, **1b**; Ar = 2,6-^{i}Pr$_2$C$_6$H$_3$). These novel complexes are thermally robust in anaerobic, anhydrous CH_2Cl_2 but decompose upon exposure to O_2 or H_2O to yield several novel organic and complex products (i.e., **2**−**4**). The organic oxidation products are consistent with formation of phenoxyl radical and reduction of O_2, which results in distinct two-electron aromatic oxidation reactions, either hydroxylation of an aromatic C−H bond on a 3-phenyl pyrazole substituent of **1a** or dihydroxylation of the phenol ring of **1b**. In contrast, oxygenation of hydrolyzed **1a**,**b** leads to relatively slow autoxidation of free phenol, although addition of H_2O_2 also gives the intramolecular aromatic hydroxylation to form **2**. Taken together, the O_2 reduction and aromatic oxidations may be relevant to TPQ generation in nickel-substituted apo-CAO and to toxicology arising from oxidative stress mediated by xenobiotic interaction of nickel with intracellular thiols and phenols.

Four different reaction mechanisms can be proposed that explain the phenol oxidation and concurrent O_2 reduction: (i) homolysis of the Ni−OAr bond leading to phenoxyl radical and Ni(I), which captures O_2;[43−45] (ii) hydrolysis of the Ni−OAr bond and autoxidation of free phenol; (iii) outer-sphere oxidation of intact phenolate complexes by O_2, followed by Ni(III)−OAr bond homolysis; or (iv) inner-sphere ligation and activation of O_2. With regard to initial Ni(II)−OAr bond homolysis (mechanism i), we clearly demonstrated the thermal stability of **1a** in dry CH_2Cl_2. Deliberate addition of H_2O to **1a**,**b** confirmed that the Ni−OAr bonds are susceptible to hydrolysis (mechanism ii); moreover, addition of H_2O_2 to hydrolyzed **1a** yielded the same product complex **2** as decomposition under O_2. However, aerobic oxidation of the free phenol was observed to be slow and inefficient. Unless phenol autoxidation is inhibited by the presence of excess H_2O, it seems necessary to propose that a majority of the oxidation chemistry observed in dry CH_2Cl_2 results from reaction of O_2 with the intact phenolate complexes. Direct O_2 reduction by **1a**,**b** might entail one-electron transfer, either by an outer-sphere mechanism to form superoxide and [TpNi−OAr]$^{\bullet+}$ radical intermediates (mechanism iii) or by formation of an inner-sphere adduct [TpNi(OAr)(O_2)] (mechanism iv). In either case, the complex intermediate would decompose by Ni(III)−OAr bond homolysis, with subsequent phenoxyl radical and reduced O_2 chemistry proceeding as already described (Scheme 2).[67]

Although nickel complex intermediates were not observed to accumulate during aerobic decompositions of **1a**,**b**, a number of possible intermediates arising along competitive oxidation and hydrolysis pathways of the TpNiOAr complexes can be proposed (Scheme 3). Hydrolyses of the starting complexes

Scheme 3

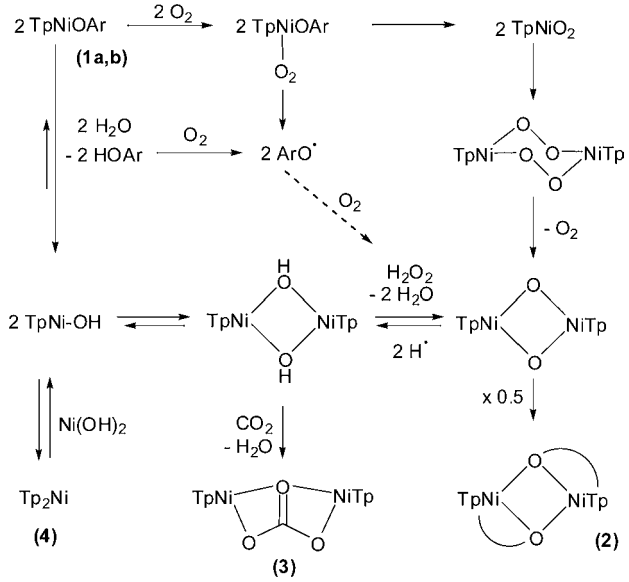

generate free phenol and intermediate [$Tp^{R,Me}$Ni−OH] species (Scheme 3, left). The latter give rise to the known dimeric complexes [$Tp^{Me,Me}$Ni(μ-OH)]$_2$ (70% spectroscopic yield)[34] and [($Tp^{Ph,Me}$)$_2$Ni] (**4**, 100% isolated yield). As demonstrated by quantitative spectroscopic conversion to **2**, the hydroxo complexes may capture H_2O_2 to form the oxidizing species [TpNi(μ-O)]$_2$; complex analogues of this intermediate have been structurally characterized and are known to decompose by intramolecular ligand oxidation.[32−34] However, phenol oxidation, and thus reduction of oxygen, was inefficient in the presence of excess water. Therefore, an alternative route to [TpNi(μ-O)]$_2$ involving direct reaction of O_2 with **1a**,**b** is proposed (Scheme 3, right). Possible electronic and geometric structures for an initial [TpNi(OPh)(O_2)] adduct, which was not observed experimentally, were obtained by DFT calculations (Figure 8B−D). As in proposed TPQ biogenesis mechanisms,[50−54] this intermediate might undergo intramolecular collapse, resulting in oxidative modification of the phenolate ring. Competing phenoxyl radical homolysis, perhaps assisted by enhanced steric contact between *ortho*-phenolate

and 3-pyrazole substituents in a high-coordinate adduct, would generate a reactive $TpNiO_2$ intermediate, for which a range of computational structures was also obtained (Figure 8E−I). Similar complexes were recently isolated and structurally characterized;[19−26] in one case, an isolated (nacnac)NiO_2 complex was found to carry out aromatic oxygenation of a 2,6-disubstituted phenol.[22] Following literature precedent, a low-spin $TpNiO_2$ complex, formally a radical species, might otherwise dimerize to generate $[TpNi(\mu\text{-}O_2)]_2$, a bis(μ-1,2-superoxo) intermediate akin to TPA-supported analogues.[24,25] O_2 extrusion would then effect net superoxide dismutation to yield a peroxo-bridged dimer $[TpNi]_2(\mu\text{-}O_2)$ akin to an analogue supported by tmc,[29] and finally the $[TpNi(\mu\text{-}O)]_2$ valence isomer, the same intermediate obtained by hydrolysis and H_2O_2 capture.[34] However, any of the proposed activated oxygen complexes (Scheme 3, right) might effect the observed aromatic oxidations.[22,24]

The $[TpNi(\mu\text{-}O)]_2$ intermediate is capable of two-electron oxidation, giving a 50% theoretical yield of modified ligand complex **2**. Therefore, isolation of **2** in 53% yield likely reflects minor turnover with residual H_2O_2 (Scheme 3, center); the yield of peroxide equivalents based on observed organic products is 56 mol % (Scheme 2). The phenolate−nickel(II) LMCT bands of **2** were partially obscured by organic products in the oxygenation reaction of **1a** (Figure 2), but the intensity of the shoulder near 317 nm was consistent with a comparable spectroscopic yield. Moreover, intramolecular C−H bond hydroxylation was reported to be relatively slow for $[Tp^{Me,Me}Ni(\mu\text{-}O)]_2$,[34] which may afford the ultimate opportunity for convergence of hydrolysis and oxygenation pathways, as well as diversion of oxidation chemistry away from the supporting Tp ligand and onto the phenol ring in the case of **1b**. In this case, the dimeric complex **3** with unmodified $Tp^{Me,Me}$ ligands was obtained in 51% isolated yield. The complex yields are thus consistent with Scheme 3; however, the mass balances of nickel complex(es) remaining after isolation of **2** and **3** and yields of organic products arising from oxygenation of **1b** were not determined. Hence, other mechanistic pathways are not excluded.

Regardless of the mechanistic details of O_2 reduction, it is clear this chemistry occurs at the expense of the phenolate moiety during decomposition of **1a**,**b**; both this chemistry and the subsequent aromatic oxidations may be relevant to nickel-catalyzed TPQ biogenesis in apo-CAO. Oxidation of **1a** leads to C−H bond hydroxylation of a 3-phenylpyrazole substituent on the supporting $Tp^{Ph,Me}$ ligand, while oxidation of **1b** leads to a different modification of the phenolate ring. Thus, another significant question remaining to be explored is the selectivity of the oxidation chemistry in the case of **1a**, where two different aromatic substrates are present and a peroxide shunt was also demonstrated.

In summary, we prepared bioinspired TpNi−OAr complexes **1a**,**b** that closely approximate the N_3O (His_3Tyr) ligand field of apo-CAO. Similar to TPQ biogenesis (Scheme 1), **1a**,**b** decompose in aerobic solutions, leading to phenoxyl radical generation, O_2 reduction, and oxidation of aromatic substrates. Hydrolysis products were identified, and subsequent phenol autoxidation and H_2O_2 activation were demonstrated. Having identified several organic and complex products in a complicated network of competitive reaction pathways (Schemes 2 and 3), we are positioned to address fundamental kinetic and mechanistic questions in future studies. Relevant issues raised by this investigation include the nature of the O_2 reduction, the identity of the reactive nickel and reduced oxygen intermediates, and how these yield the divergent oxidative modifications of aromatic substrates.

■ ASSOCIATED CONTENT

Supporting Information

Details of the reactions, product characterizations, and DFT calculations; and X-ray crystallographic data for **1a**, **1b**, and **2**−**4**. This material is available free of charge via the Internet at http://pubs.acs.org.

■ AUTHOR INFORMATION

Corresponding Author

*E-mail: jensenm@ohio.edu.

Notes

The authors declare no competing financial interest.

■ ACKNOWLEDGMENTS

The authors acknowledge the donors of the American Chemical Society Petroleum Research Fund (49296-DNI3) for support of this research. We also thank the Ohio University 1804 Fund for support in acquiring the hardware and software for DFT computations.

■ REFERENCES

(1) Sono, M.; Roach, M. P.; Coulter, E. D.; Dawson, J. H. *Chem. Rev.* **1996**, *96*, 2841−2888.
(2) Costas, M.; Mehn, M. P.; Jensen, M. P.; Que, L., Jr. *Chem. Rev.* **2004**, *104*, 939−986.
(3) Kovaleva, E. G.; Neibergall, M. B.; Chakrabarty, S.; Lipscomb, J. D. *Acc. Chem. Res.* **2007**, *40*, 475−483.
(4) Krebs, C.; Fujimori, D. G.; Walsh, C. T.; Bollinger, J. M., Jr. *Acc. Chem. Res.* **2007**, *40*, 484−492.
(5) Tshuva, E. Y.; Lippard, S. J. *Chem. Rev.* **2004**, *104*, 987−1012.
(6) Decker, A.; Solomon, E. I. *Curr. Opin. Chem. Biol.* **2005**, *9*, 152−163.
(7) Korendovych, I. V.; Kryatov, S. V.; Rybak-Akimova, E. V. *Acc. Chem. Res.* **2007**, *40*, 510−521.
(8) Mirica, L. M.; Ottenwaelder, X.; Stack, T. D. P. *Chem. Rev.* **2004**, *104*, 1013−1046.
(9) Lewis, E. A.; Tolman, W. B. *Chem. Rev.* **2004**, *104*, 1047−1076.
(10) Kim, E.; Chufán, E. E.; Kamaraj, K.; Karlin, K. D. *Chem. Rev.* **2004**, *104*, 1077−1134.
(11) Ju, T.; Goldsmith, R. B.; Chai, S. C.; Maroney, M. J.; Pochapsky, S. S.; Pochapsky, T. C. *J. Mol. Biol.* **2006**, *363*, 823−834.
(12) Szajna, E.; Arif, A. M.; Berreau, L. M. *J. Am. Chem. Soc.* **2005**, *127*, 17186−17187.
(13) Kimura, E.; Sakonaka, A.; Machida, R.; Kodama, M. *J. Am. Chem. Soc.* **1982**, *104*, 4255−4257.
(14) Edison, S. E.; Hotz, R. P.; Baldwin, M. J. *Chem. Commun.* **2004**, 1212−1213.
(15) Koola, J. D.; Kochi, J. K. *Inorg. Chem.* **1987**, *26*, 908−916.
(16) Kinneary, J. F.; Albert, J. S.; Burrows, C. J. *J. Am. Chem. Soc.* **1988**, *110*, 6124−6129.
(17) Nagataki, T.; Tachi, Y.; Itoh, S. *Chem. Commun.* **2006**, 4016−4018.
(18) Grapperhaus, C. A.; Darensbourg, M. Y. *Acc. Chem. Res.* **1998**, *31*, 451−459.
(19) Fujita, K.; Schenker, R.; Gu, W.; Brunold, T. C.; Cramer, S. P.; Riordan, C. G. *Inorg. Chem.* **2004**, *43*, 3324−3326.
(20) Kieber-Emmons, M. T.; Annaraj, J.; Seo, M. S.; Van Heuvelen, K. M.; Tosha, T.; Kitagawa, T.; Brunold, T. C.; Nam, W.; Riordan, C. G. *J. Am. Chem. Soc.* **2006**, *128*, 14230−14231.
(21) Yao, S.; Bill, E.; Milsmann, C.; Wieghardt, K.; Driess, M. *Angew. Chem., Int. Ed.* **2008**, *47*, 7110−7113.

(22) Company, A.; Yao, S.; Ray, K.; Driess, M. *Chem.–Eur. J* **2010**, *16*, 9669–9675.
(23) Pietrzyk, P.; Podolska, K.; Mazur, T.; Sojka, Z. *J. Am. Chem. Soc.* **2011**, *133*, 19931–19943.
(24) Shiren, K.; Ogo, S.; Fujinami, S.; Hayashi, H.; Suzuki, M.; Uehara, A.; Watanabe, Y.; Moro-oka, Y. *J. Am. Chem. Soc.* **2000**, *122*, 254–262.
(25) Cho, J.; Furutachi, H.; Fujinami, S.; Tosha, T.; Ohtsu, H.; Ikeda, O.; Suzuki, A.; Nomura, M.; Uruga, T.; Tanida, H.; Kawai, T.; Tanaka, K.; Kitagawa, T.; Suzuki, M. *Inorg. Chem.* **2006**, *45*, 2873–2885.
(26) Cho, J.; Sarangi, R.; Annaraj, J.; Kim, S. Y.; Kubo, M.; Ogura, T.; Solomon, E. I.; Nam, W. *Nat. Chem.* **2009**, *1*, 568–572.
(27) Cho, J.; Furutachi, H.; Fujinami, S.; Suzuki, M. *Angew. Chem., Int. Ed.* **2004**, *43*, 3300–3303.
(28) Kieber-Emmons, M. T.; Schenker, R.; Yap, G. P. A.; Brunold, T. C.; Riordan, C. G. *Angew. Chem., Int. Ed.* **2004**, *43*, 6716–6718.
(29) Schenker, R.; Kieber-Emmons, M. T.; Riordan, C. G.; Brunold, T. C. *Inorg. Chem.* **2005**, *44*, 1752–1762.
(30) Hikichi, S.; Kobayashi, C.; Yoshizawa, M.; Akita, M. *Chem.–Asian J* **2010**, *5*, 2086–2092.
(31) Hikichi, S.; Okuda, H.; Ohzu, Y.; Akita, M. *Angew. Chem., Int. Ed.* **2009**, *48*, 188–191.
(32) Hikichi, S.; Yoshizawa, M.; Sasakura, Y.; Akita, M.; Moro-oka, Y. *J. Am. Chem. Soc.* **1998**, *120*, 10567–10568.
(33) Hikichi, S.; Yoshizawa, M.; Sasakura, Y.; Komatsuzaki, H.; Akita, M.; Moro-oka, Y. *Chem. Lett.* **1999**, 979–980.
(34) Hikichi, S.; Yoshizawa, M.; Sasakura, Y.; Komatsuzaki, H.; Moro-oka, Y.; Akita, M. *Chem.–Eur. J* **2001**, *7*, 5011–5028.
(35) Itoh, S.; Bandoh, H.; Nagatomo, S.; Kitagawa, T.; Fukuzumi, S. *J. Am. Chem. Soc.* **1999**, *121*, 8945–8946.
(36) Itoh, S.; Bandoh, H.; Nakagawa, M.; Nagatomo, S.; Kitagawa, T.; Karlin, K. D.; Fukuzumi, S. *J. Am. Chem. Soc.* **2001**, *123*, 11168–11178.
(37) Bag, B.; Mondal, N.; Rosair, G.; Mitra, S. *Chem. Commun.* **2000**, 1729–1730.
(38) Mandimutsira, B. S.; Yamarik, J. L.; Brunold, T. C.; Gu, W.; Cramer, S. P.; Riordan, C. G. *J. Am. Chem. Soc.* **2001**, *123*, 9194–9195.
(39) Schenker, R.; Mandimutsira, B. S.; Riordan, C. G.; Brunold, T. C. *J. Am. Chem. Soc.* **2002**, *124*, 13842–13855.
(40) Honda, K.; Cho, J.; Matsumoto, T.; Roh, J.; Furutachi, H.; Tosha, T.; Kubo, M.; Fujinami, S.; Ogura, T.; Kitagawa, T.; Suzuki, M. *Angew. Chem., Int. Ed.* **2009**, *48*, 3304–3307.
(41) Kunishita, A.; Doi, Y.; Kubo, M.; Ogura, T.; Sugimoto, H.; Itoh, S. *Inorg. Chem.* **2009**, *48*, 4997–5004.
(42) Tano, T.; Doi, Y.; Inosako, M.; Kunishita, A.; Kubo, M.; Ishimaru, H.; Ogura, T.; Sugimoto, H.; Itoh, S. *Bull. Chem. Soc. Jpn.* **2010**, *83*, 530–538.
(43) Yao, S.; Driess, M. *Acc. Chem. Res.* **2012**, *45*, 276–287.
(44) Kieber-Emmons, M. T.; Riordan, C. G. *Acc. Chem. Res.* **2007**, *40*, 618–625.
(45) Suzuki, M. *Acc. Chem. Res.* **2007**, *40*, 609–617.
(46) Cheng, C.-C.; Rokita, S. E.; Burrows, C. J. *Angew. Chem., Int. Ed. Engl.* **1993**, *32*, 277–278.
(47) Liang, Q.; Ananias, D. C.; Long, E. C. *J. Am. Chem. Soc.* **1998**, *120*, 248–257.
(48) Kasprzak, K. S.; Salnikow, K. *Met. Ions Life Sci.* **2007**, *2*, 619–660.
(49) Kim, M.; Okajima, T.; Kishishita, S.; Yoshimura, M.; Kawamori, A.; Tanizawa, K.; Yamaguchi, H. *Nat. Struct. Biol.* **2002**, *9*, 591–596.
(50) DuBois, J. L.; Klinman, J. P. *Biochemistry* **2005**, *44*, 11381–11388.
(51) Prabhakar, R.; Siegbahn, P. E. M. *J. Am. Chem. Soc.* **2004**, *126*, 3996–4006.
(52) Ghosh, S.; Cirera, J.; Vance, M. A.; Ono, T.; Fujisawa, K.; Solomon, E. I. *J. Am. Chem. Soc.* **2008**, *130*, 16262–16273.
(53) Okajima, T.; Kishishita, S.; Chiu, Y.-C.; Murakawa, T.; Kim, M.; Yamaguchi, H.; Hirota, S.; Kuroda, S.; Tanizawa, K. *Biochemistry* **2005**, *44*, 12041–12048.
(54) Samuels, N. M.; Klinman, J. P. *Biochemistry* **2005**, *44*, 14308–14317.
(55) Fujisawa, K.; Iwata, Y.; Kitajima, N.; Higashimura, H.; Kubota, M.; Miyashita, Y.; Yamada, Y.; Okamoto, K.; Moro-oka, Y. *Chem. Lett.* **1999**, 739–740.
(56) Jazdzewski, B. A.; Holland, P. L.; Pink, M.; Young, V. G., Jr.; Spencer, D. J. E.; Tolman, W. B. *Inorg. Chem.* **2001**, *40*, 6097–6107.
(57) Gorelsky, S. I.; Basumallick, L.; Vura-Weis, J.; Sarangi, R.; Hodgson, K. O.; Hedman, B.; Fujisawa, K.; Solomon, E. I. *Inorg. Chem.* **2005**, *44*, 4947–4960.
(58) Chattopadhyay, S.; Deb, T.; Ma, H.; Petersen, J. L.; Young, V. G., Jr.; Jensen, M. P. *Inorg. Chem.* **2008**, *47*, 3384–3392.
(59) Chattopadhyay, S.; Deb, T.; Petersen, J. L.; Young, V. G., Jr.; Jensen, M. P. *Inorg. Chem.* **2010**, *49*, 457–467.
(60) Desrochers, P. J.; Cutts, R. W.; Rice, P. K.; Golden, M. L.; Graham, J. B.; Barclay, T. M.; Cordes, A. W. *Inorg. Chem.* **1999**, *38*, 5690–5694.
(61) Nakazawa, J.; Ogiwara, H.; Kashiwazaki, Y.; Ishii, A.; Imamura, N.; Samejima, Y.; Hikichi, S. *Inorg. Chem.* **2011**, *50*, 9933–9935.
(62) Rheingold, A. L.; Ostrander, R. L.; Haggerty, B. S.; Trofimenko, S. *Inorg. Chem.* **1994**, *33*, 3666–3676.
(63) Trofimenko, S. *J. Am. Chem. Soc.* **1967**, *89*, 6288–6294.
(64) Tabuchi, K.; Ertem, M. Z.; Sugimoto, H.; Kunishita, A.; Tano, T.; Fujieda, N.; Cramer, C. J.; Itoh, S. *Inorg. Chem.* **2011**, *50*, 1633–1647.
(65) Santi, R.; Romano, A. M.; Sommazzi, A.; Grande, M.; Bianchini, C.; Mantovani, G. *J. Mol. Catal. A* **2005**, *229*, 191–197.
(66) Uehara, K.; Hikichi, S.; Akita, M. *J. Chem. Soc., Dalton Trans.* **2002**, 3529–3538.
(67) Evans, D. F.; Jakubovic, D. A. *J. Chem. Soc., Dalton Trans.* **1988**, 2927–2933.
(68) Heyne, B.; Kohnen, S.; Brault, D.; Mouithys-Mickalad, A.; Tfibel, F.; Hans, P.; Fontaine-Aupart, M.-P.; Hoebeke, M. *Photochem. Photobiol. Sci.* **2003**, *2*, 939–945.
(69) *ADF 2008.01*; Scientific Computing and Modelling NV; Vrije Universiteit: Amsterdam, Netherlands, 2008.
(70) te Velde, G.; Bickelhaupt, F. M.; Baerends, E. J.; Fonseca Guerra, C.; van Gisbergen, S. J. A.; Snijders, J. G.; Ziegler, T. *J. Comput. Chem.* **2001**, *22*, 931–967.
(71) Vosko, S. H.; Wilk, L.; Nusair, M. *Can. J. Phys.* **1980**, *58*, 1200–1211.
(72) Becke, A. D. *Phys. Rev.* **1988**, *A38*, 3098–3100.
(73) Perdew, J. P. *Phys. Rev.* **1986**, *B33*, 8822–8824.
(74) *APEX II*; Bruker Analytical X-ray Systems: Madison, WI, 2001.
(75) An empirical correction for absorption anisotropy: Blessing, R. H. *Acta Crystallogr.* **1995**, *A51*, 33–38.
(76) *SAINT+*, V7.68; Bruker Analytical X-Ray Systems: Madison, WI, 2003.
(77) *SHELXTL*, V2008/4; Bruker Analytical X-Ray Systems: Madison, WI, 2008.
(78) *Mercury*, 3.0; Cambridge Crystallographic Data Centre: Cambridge, U.K., 2011.
(79) Ruman, T.; Ciunik, Z.; Szklanny, E.; Wołowiec, S. *Polyhedron* **2002**, *21*, 2743–2753.
(80) Kharasch, M. S.; Joshi, B. S. *J. Org. Chem.* **1957**, *22*, 1439–1443.
(81) Yang, L.; Powell, D. R.; Houser, R. P. *Dalton Trans.* **2007**, 955–964.
(82) Desrochers, P. J.; LeLievre, S.; Johnson, R. J.; Lamb, B. T.; Phelps, A. L.; Cordes, A. W.; Gu, W.; Cramer, S. P. *Inorg. Chem.* **2003**, *42*, 7945–7950.
(83) Northcutt, T. O.; Lachicotte, R. J.; Jones, W. D. *Organometallics* **1998**, *17*, 5148–5152.
(84) Desrochers, P. J.; Telser, J.; Zvyagin, S. A.; Ozarowski, A.; Krzystek, J.; Vicic, D. A. *Inorg. Chem.* **2006**, *45*, 8930–8941.
(85) Addison, A. W.; Rao, T. N.; Reedijk, J.; van Rijn, J.; Verschoor, G. C. *J. Chem. Soc., Dalton Trans.* **1984**, 1349–1356.
(86) Fujisawa, K.; Tada, N.; Nishida, Y.; Miyashita, Y.; Okamoto, K. *Inorg. Chem. Commun.* **2008**, *11*, 381–384.

(87) Mehn, M. P.; Fujisawa, K.; Hegg, E. L.; Que, L., Jr. *J. Am. Chem. Soc.* **2003**, *125*, 7828−7842.
(88) Higgs, T. C.; Carrano, C. J. *Inorg. Chem.* **1997**, *36*, 298−306.
(89) Kitajima, N.; Hikichi, S.; Tanaka, M.; Moro-oka, Y. *J. Am. Chem. Soc.* **1993**, *115*, 5496−5508.
(90) Trofimenko, S.; Rheingold, A. L.; Liable Sands, L. M. *Inorg. Chem.* **2002**, *41*, 1889−1896.
(91) Janiak, C.; Temizdemir, S.; Dechert, S.; Deck, W.; Girgsdies, F.; Heinze, J.; Kolm, M. J.; Scharmann, T. G.; Zipffel, O. M. *Eur. J. Inorg. Chem.* **2000**, 1229−1241.
(92) Bandoli, G.; Clemente, D. A.; Paolucci, G.; Doretti, L. *Cryst. Struct. Commun.* **1979**, *8*, 965−970.
(93) Cecchi, P.; Gioia Lobbia, G.; Marchetti, F.; Valle, G.; Calogero, S. *Polyhedron* **1994**, *13*, 2173−2178.
(94) Desrochers, P. J.; Brown, J. R.; Arvin, M. E.; Jones, G. D.; Vicic, D. A. *Acta Crystallogr.* **2005**, *E61*, m1455−m1458.
(95) Calabrese, J. C.; Trofimenko, S. *Inorg. Chem.* **1992**, *31*, 4810−4814.
(96) Santana, M. D.; López-Banet, L.; García, G.; García, L.; Pérez, J.; Liu, M. *Eur. J. Inorg. Chem.* **2008**, 4012−4018.
(97) Hammes, B. S.; Luo, X.; Chohan, B. S.; Carrano, M. W.; Carrano, C. J. *J. Chem. Soc., Dalton Trans.* **2002**, 3374−3380.
(98) Adams, H.; Batten, S. R.; Davies, G. M.; Duriska, M. B.; Jeffery, J. C.; Jensen, P.; Lu, J.; Motson, G. R.; Coles, S. J.; Hursthouse, M. B.; Ward, M. D. *Dalton Trans.* **2005**, 1910−1923.
(99) Batten, S. R.; Duriska, M. B.; Jensen, P.; Lu, J. *Aust. J. Chem.* **2007**, *60*, 72−74.
(100) Jesson, J. P.; Trofimenko, S.; Eaton, D. R. *J. Am. Chem. Soc.* **1967**, *89*, 3148−3158.
(101) Fulmer, G. R.; Miller, A. J. M.; Sherden, N. H.; Gottlieb, H. E.; Nudelman, A.; Stoltz, B. M.; Bercaw, J. E.; Goldberg, K. I. *Organometallics* **2010**, *29*, 2176−2179.